Title
Design and simulation of origami structures with smooth folds

Journal
Proceedings of the Royal Society A, 473(2200)

ISSN
1364-5021

Authors
Hernandez, EA Peraza
Hartl, DJ
Lagoudas, DC

Publication Date
2017-04-01

DOI
10.1098/rspa.2016.0716

Peer reviewed

PROCEEDINGS A

rspa.royalsocietypublishing.org

Research

Cite this article: Peraza Hernandez EA, Hartl DJ, Lagoudas DC. 2017 Design and simulation of origami structures with smooth folds. *Proc. R. Soc. A* **473**: 20160716.
http://dx.doi.org/10.1098/rspa.2016.0716

Received: 20 September 2016
Accepted: 27 March 2017

Subject Areas:
computer-aided design

Keywords:
origami, design, smooth folds

Author for correspondence:
D. C. Lagoudas
e-mail: lagoudas@tamu.edu

Electronic supplementary material is available online at https://dx.doi.org/10.6084/m9.figshare.c.3738167.

THE ROYAL SOCIETY PUBLISHING

Design and simulation of origami structures with smooth folds

E. A. Peraza Hernandez[1], D. J. Hartl[1] and D. C. Lagoudas[1,2]

[1]Department of Aerospace Engineering, and [2]Department of Materials Science and Engineering, Texas A&M University, College Station, TX 77843, USA

DJH, 0000-0001-9922-0481

Origami has enabled new approaches to the fabrication and functionality of multiple structures. Current methods for origami design are restricted to the idealization of folds as creases of zeroth-order geometric continuity. Such an idealization is not proper for origami structures of non-negligible fold thickness or maximum curvature at the folds restricted by material limitations. For such structures, folds are not properly represented as creases but rather as bent regions of higher-order geometric continuity. Such fold regions of arbitrary order of continuity are termed as *smooth folds*. This paper presents a method for solving the following origami design problem: given a goal shape represented as a polygonal mesh (termed as the *goal mesh*), find the geometry of a single planar sheet, its pattern of smooth folds, and the history of folding motion allowing the sheet to approximate the goal mesh. The parametrization of the planar sheet and the constraints that allow for a valid pattern of smooth folds are presented. The method is tested against various goal meshes having diverse geometries. The results show that every determined sheet approximates its corresponding goal mesh in a known folded configuration having fold angles obtained from the geometry of the goal mesh.

1. Introduction

Origami, the ancient art of folding initially planar sheets into diverse shapes, has gathered increasing attention from researchers in various fields [1–3]. Origami offers engineers novel ways to fabricate,

assemble, store and morph structures [4,5]. Potential engineering advantages of origami-inspired structures include compact storage/deployment capabilities [6,7], potential for reconfigurability [8–10], and reduction in manufacturing complexity [11,12]. Applications of origami-inspired structures include: various space structures [13], electronic components [14], robots [15], shelters [16], biomedical devices [17] and many others [4,18].

The study of the kinematics of origami structures is an active research topic and has been investigated by various researchers [19]. Two main assumptions have been made in the development of mathematical models for the kinematics of origami structures to date [19–21]: that folds are straight creases having zeroth-order geometric continuity (termed as *creased folds*), and that planar faces bounded by the folds and the sheet boundary are rigid (i.e. these faces are neither bent nor stretched). For example, Belcastro & Hull [20,21] presented a model for origami structures having creased folds and rigid faces derived by representing the deformation associated with folding using affine transformations.

Creating an origami structure having desired characteristics, a desired shape in particular, is known as *origami design* [22]. Origami design is a challenge encountered not only by origami artists but also by designers and engineers who apply origami in various fields. Before obtaining extensive interest from various research communities, most origami design was performed through trial and error or other heuristic approaches based on the intuition of an artist or designer [23]. With the increase in complexity of origami shapes that provide engineering utility, computational methods for the design of origami structures have become essential for developments in this area of study [1,5,23]. As in most kinematic models for origami structures, current methods for origami design consider rigid faces and creased folds [24,25]. For example, one of the most well-known methods for origami design is the *tree method* [23]. The tree method generates a pattern of creased folds on a squared sheet that allows for the folding of the sheet into a *base*, a folded shape whose projection to a plane is the tree line graph of the goal shape.

A method for determining the geometry and pattern of creased folds associated with a planar sheet that can fold towards a goal polyhedral surface is termed as *unfolding polyhedra* [1,26]. The objective in this method is to determine an *unfolding* of the goal polyhedral surface [1]. An unfolding is defined as the flattening of the goal polyhedral surface to a plane such that the surface becomes a planar polygon having boundary segments that correspond to cuts made on the polyhedral surface [1]. Generally, the unfolding must be a single simply connected polygon having no overlaps and the cuts must correspond to edges of the goal polyhedral surface. A drawback of this approach is that it has been demonstrated that there are non-convex polyhedra which do not have unfoldings with the mentioned characteristics [1]. It also remains an open question whether the method of unfolding polyhedra works for any goal convex polyhedral surface [1].

The currently available method for origami design applicable to the widest range of goal shapes was introduced by Tachi in [22,27]. In such studies, Tachi presented a method for obtaining a pattern of creased folds in a convex planar sheet that folds into an arbitrary three-dimensional goal shape represented as a polygonal mesh [22,27,28]. The method is based on the introduction of regions having two rigid faces and three creased folds placed between any two faces of the polygonal mesh connected by an interior edge. The creased folds are used to *tuck* fold such introduced regions to form the three-dimensional polygonal mesh starting from a planar sheet [27]. This method is shown to successfully work on goal polygonal meshes (convex and non-convex) of various complexities in terms of number of faces and non-regular connectivity.

Although the aforementioned kinematic models for origami and methods for origami design (among other more recent ones [25,29]) allow for the simulation and design of origami structures having various complexities, they assume that the sheet only contains creased folds. Such a simplification may not be appropriate for structures having non-negligible fold thickness or constructed from materials that do not provide sufficient strain magnitudes for a creased idealization. Examples of these structures include foldable thick metallic sheets [30] and self-folding sheets having actuation provided by active materials such as shape memory alloys (SMAs) [31] and shape memory polymers (SMPs) [32]. For structures having such characteristics,

the folded regions are not properly represented as creases but instead as *bent* regions in the sheet exhibiting higher-order geometric continuity. These bent regions of arbitrary order of geometry continuity are termed herein as *smooth folds* [33,34].

In the modelling and design approaches for origami considered here, the previously mentioned assumption of rigid faces is maintained while the assumption of creased folds is replaced by the introduction of smooth folds. A model for the kinematics of origami structures with smooth folds and rigid faces was fully addressed by the authors in [33]. There, a detailed description of the geometry of smooth folds having arbitrary order of geometric continuity and their associated kinematic variables were provided. Kinematic constraints for such variables allowing for valid configurations were also presented. In addition, the mapping between reference and current configurations fully determined by the kinematic variables of the smooth folds was also derived. Finally, Peraza *et al.* [33] provides an approach for kinematic simulation of origami structures with smooth folds having arbitrary reference configuration and subject to arbitrary folding motion. Such a model and simulation approach are described in more detail in §2. In [34], the authors presented a model for the elastic response of origami structures with smooth folds. However, the design of origami structures considering smooth folds has not been addressed in the aforementioned studies [33,34].

The main contribution of this work is a novel method for origami design having its inspiration from that presented by Tachi in [22,27] but considering smooth folds as opposed to creased folds. The method aims to solve the following origami design problem: given a goal shape represented as a polygonal mesh (the *goal mesh*), find the geometry of a single continuous planar sheet, its pattern of *smooth folds*, and a history of folding motion from the determined planar sheet configuration to a folded configuration that approximates the goal mesh. A process for determining a history of folding motion from the determined planar sheet configuration to the folded configuration that approximates the goal mesh has not been previously addressed in [22,27]. Therefore, the determination of such a history of folding motion addressed here represents another contribution of this work and is applicable to both origami with smooth folds and conventional origami with creased folds. The present method for origami design can be applied to foldable thick metallic sheets [30], self-folding sheets with actuation provided by active materials [31,32], and other structures having localized deformation at bent folded regions [35]. A method for designing planar sheets having bent folds that allow for approximation of three-dimensional goal meshes was presented in [36]. There, given a three-dimensional goal mesh, the method determines an approximating developable mesh by altering node positions and cutting certain edges. The design method presented here also considers smooth folds and requires certain modifications of the given goal mesh. However, the mesh modifications executed in this work do not provide an approximate developable mesh but rather exist only to accommodate smooth folds (refer to §4a). The normal vectors and the corner angles of the original goal mesh faces and the modified faces are identical in the present method, in contrast with the method presented in [36].

The outline of this paper is as follows: a review of the main aspects of the kinematic model for origami with smooth folds presented by the authors in [33] is provided in §2. The description of the origami design problem addressed here is presented in §3. The novel design method for origami with smooth folds proposed in this work is described in detail in §4. A numerical procedure used to determine valid planar sheet designs is outlined in §5. Further discussion of the presented method for origami design is provided in §6. A description of the process for obtaining a history of folding motion allowing the determined sheet to approximate the goal mesh is presented in §7. Results illustrating the capabilities of the proposed design method are presented in §8 and concluding remarks are provided in §9.

2. Kinematics of origami structures with smooth folds

The main definitions and aspects of origami with smooth folds are briefly reviewed in this section. A detailed description of a modelling approach for origami with smooth folds is provided in [33]. The continuum body considered in origami with smooth folds is denoted as the *sheet* and is

a three-dimensional, path-connected, orientable surface with boundary. The sheet is divided into various surface sub-domains denoted as the *faces* and the *smooth folds*. The orthonormal vectors $\mathbf{e}_i \in \mathbb{R}^3$, $i \in \{1,2,3\}$, with $\mathbf{e}_3 := \mathbf{e}_1 \times \mathbf{e}_2$ form the basis $\{\mathbf{e}_1, \mathbf{e}_2, \mathbf{e}_3\}$ that defines the fixed global coordinate system. The *reference configuration* of the sheet is denoted $\mathcal{S}_0$ and is defined such that it is contained in the plane spanned by $\mathbf{e}_1$ and $\mathbf{e}_2$ with its surface sub-domains not overlapping each other. The configuration of the faces and the smooth folds in $\mathcal{S}_0$ are, respectively, denoted as $\mathcal{F}_0^i$, $\mathcal{P}_0^j \subset \mathcal{S}_0, i \in \{1,\ldots,N_\mathcal{F}\}$, $j \in \{1,\ldots,N_\mathcal{P}\}$ (where $N_\mathcal{F}$ and $N_\mathcal{P}$ are the number of smooth folds and faces in the sheet, respectively). Therefore, $\mathcal{S}_0 = (\bigcup_{i=1}^{N_\mathcal{F}} \mathcal{F}_0^i) \cup (\bigcup_{i=1}^{N_\mathcal{P}} \mathcal{P}_0^i)$. The side of $\mathcal{S}_0$ with normal $\mathbf{e}_3$ is selected as the positive side of the sheet. A *current configuration* of the sheet is denoted as $\mathcal{S}_t$, where the parameter t indicates the history of deformation from the reference configuration ($t = 0$) to a current configuration ($t > 0$). The configuration of the faces and the smooth folds in $\mathcal{S}_t$ are, respectively, denoted as $\mathcal{F}_t^i, \mathcal{P}_t^j \subset \mathcal{S}_t, i \in \{1,\ldots,N_\mathcal{F}\}, j \in \{1,\ldots,N_\mathcal{P}\}$ (i.e. $\mathcal{S}_t = (\bigcup_{i=1}^{N_\mathcal{F}} \mathcal{F}_t^i) \cup (\bigcup_{i=1}^{N_\mathcal{P}} \mathcal{P}_t^i)$). The following definition of valid configurations is then introduced:

Definition 2.1 (Valid configuration [33]). A *valid* current configuration $\mathcal{S}_t$ has the following characteristics: (i) the faces have undergone only rigid deformations (i.e. they are neither bent nor stretched), (ii) the sheet is not torn (initially joined surface sub-domains of the sheet remain joined), and (iii) the sheet does not self-intersect.

(a) Geometry of smooth folds

Definition 2.2 (Smooth folds). The *smooth folds* are ruled surfaces of the following form [33]:

$$\boldsymbol{\mathcal{F}}_t^i(\zeta_1,\zeta_2) = \mathbf{c}_t^i(\zeta_1) + \zeta_2 \mathbf{h}_t^i, \quad \frac{\mathrm{d}\mathbf{c}_t^i(\zeta_1)}{\mathrm{d}\zeta_1} \cdot \mathbf{h}_t^i = 0, \tag{2.1}$$

where $\boldsymbol{\mathcal{F}}_t^i(\zeta_1,\zeta_2) \in \mathbb{R}^3$ is a parametrization of the smooth fold surface $\mathcal{F}_t^i$. Without loss of generality, the parameters ζ_1 and ζ_2 are contained in the intervals $[-1,1]$ and $[0,1]$, respectively.

An example of a smooth fold is shown in figure 1. The vector $\mathbf{h}_t^i \in \mathbb{R}^3$ provides the direction of the rulings comprising $\mathcal{F}_t^i$ while the parametric curve $\mathbf{c}_t^i(\zeta_1) : [-1,1] \to \mathbb{R}^3$ defines the cross section of $\mathcal{F}_t^i$. The parametric curve $\mathbf{c}_t^i(\zeta_1)$ is contained in a plane orthogonal to $\mathbf{h}_t^i$ as stated in equation (2.1). It is further assumed that $\|\mathbf{h}_t^i\|$ is constant[1]. Therefore, the only non-rigid deformations allowed for the smooth folds are achieved through continuous bending or stretching of its cross section defined by $\mathbf{c}_t^i(\zeta_1)$. To simplify the notation, the dependence of $\boldsymbol{\mathcal{F}}_t^i(\zeta_1,\zeta_2)$, $\mathbf{c}_t^i(\zeta_1)$ and $\mathbf{h}_t^i$ on t is taken as implicit for the remainder of the paper.

Remark 2.3. Creased folds are a special case of the more general smooth folds. Specifically, creased folds are obtained when the curve parametrized by $\mathbf{c}^i(\zeta_1)$ is degenerated to a single point thereby degenerating the smooth fold surface $\mathcal{F}_t^i$ to a single straight line segment. Thus, all the contributions of this work are also applicable to conventional origami with creased folds as a special case.

A non-rigid deformation of the sheet is achieved by rotating pairs of faces joined to smooth folds relative to one another in such a manner that the sheet only attains valid configurations during this deformation. One of the kinematic variables associated with a smooth fold describes the relative rotation between the two faces joined by such a fold and is denoted as the *fold angle* (figure 1):

Definition 2.4 (Fold angle). The *fold angle* $\hat{\theta}_i(t)$ is defined as π minus the dihedral angle between the positive sides of the two faces joined to the ith smooth fold.

The dependence of the fold angles on t is taken as implicit for the remainder of the paper unless otherwise noted. As the faces of the origami structures are assumed planar and rigid (see Definition 2.1), the order of geometry continuity of the origami structures is considered in

[1] $\|\cdot\|$ denotes the two-norm of a vector, i.e. $\|\mathbf{y}\| = (\mathbf{y}\cdot\mathbf{y})^{1/2}$.

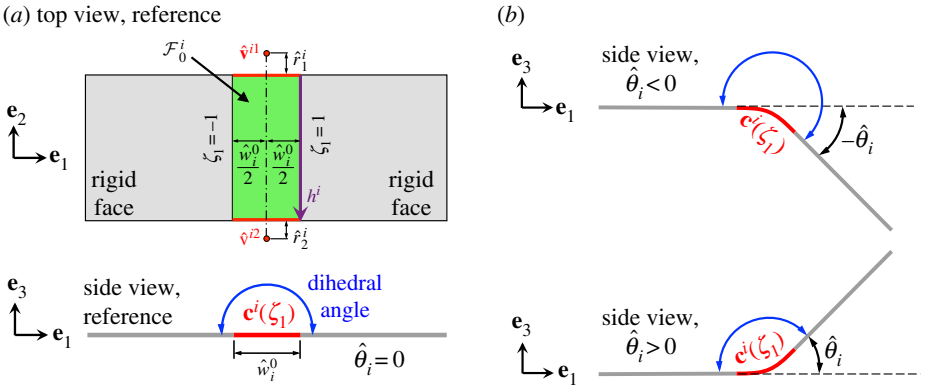

Figure 1. Schematics showing (*a*) the reference configuration and (*b*) current configurations of a smooth fold. (Online version in colour.)

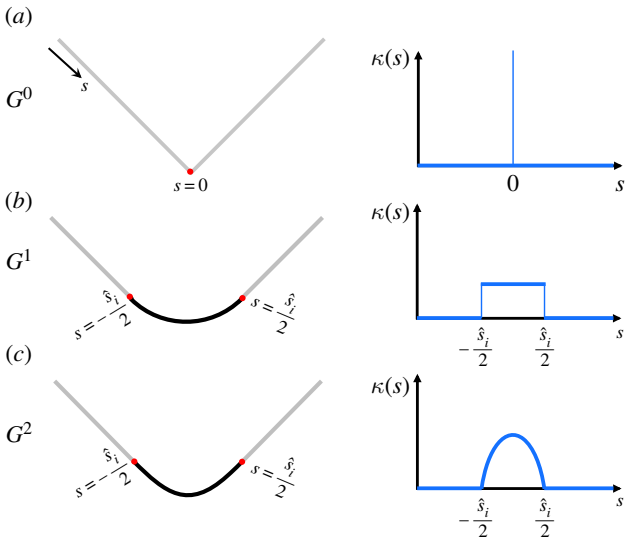

Figure 2. Schematics showing fold cross sections of various orders of geometric continuity and their associated signed curvature fields. (Online version in colour.)

the order of continuity of the smooth fold cross sections parametrized by $\mathbf{c}^i(\zeta_1)$, $i \in \{1, \ldots, N_{\mathcal{F}}\}$. Continuity conditions and parametric formulations of the curves $\mathbf{c}^i(\zeta_1)$ for various orders of geometric continuity are provided in [33]. Schematics of folds having various orders of geometric continuity and their associated signed curvature fields $\kappa(s)$ as functions of arc-length are shown in figure 2. Only continuity of position is required for G^0 continuity (figure 2*a*). Such a case corresponds to conventional creased folds. Continuity of position and tangent vector is required for G^1 continuity (figure 2*b*) [37]. Continuity of position, tangent vector and signed curvature is required for G^2 continuity (figure 2*c*). Structures having discontinuities of thickness and/or materials at the interface between the faces and the smooth folds would exhibit discontinuities in curvature at such location and thus would have G^1 continuity (figure 2*b*) while those without such discontinuities would have G^2 continuity (figure 2*c*).

The total arc-length of a fold is denoted as $\hat{s}_i$. If the curve $\mathbf{c}^i(\zeta_1)$ is reparametrized by arc-length s, the following relation between fold angle $\hat{\theta}_i$ and the curvature field of the fold cross section holds:

$$\hat{\theta}_i = \int_{-\hat{s}_i/2}^{\hat{s}_i/2} \kappa(s)\, \mathrm{d}s. \tag{2.2}$$

The current distance between the endpoints of $\mathbf{c}^i(\zeta_1)$ and is denoted as $\hat{w}_i$

$$\hat{w}_i := \|\mathbf{c}^i(1) - \mathbf{c}^i(-1)\|, \tag{2.3}$$

and the *fold width* is denoted $\hat{w}_i^0$ and is defined as the value of $\hat{w}_i$ in the reference configuration. The reference configuration of the smooth fold $\mathcal{F}_0^i$ can be fully defined by the endpoints of its fold centerline (termed as *vertices* [33]) having position vectors $\hat{\mathbf{v}}^{ij} \in \mathrm{span}(\mathbf{e}_1, \mathbf{e}_2)$, $j \in \{1, 2\}$, the fold width $\hat{w}_i^0$, and the length parameters $\hat{r}_j^i$, $j = 1, 2$ (refer to figure 1*a*). For simplicity in the simulation of origami with smooth folds, assumptions on the extensibility and curvature field of the curve $\mathbf{c}^i(\zeta_1)$ are taken such that the overall deformation of a smooth fold becomes solely a function of its fold angle $\hat{\theta}_i$. As such, the configuration of the sheet is fully defined by the set of fold angles $\{\hat{\theta}_i \mid i \in \{1, \ldots, N_{\mathcal{F}}\}\}$. The vector $\hat{\boldsymbol{\theta}} \in \mathbb{R}^{N_{\mathcal{F}}}$ is constructed by collecting the fold angles of the sheet as follows:

$$\hat{\boldsymbol{\theta}} := [\hat{\theta}_1 \ldots \hat{\theta}_{N_{\mathcal{F}}}]^\top. \tag{2.4}$$

(b) Constraints

As in conventional origami with creased folds [20,21], constraints are required for origami with smooth folds to ensure that every current configuration $\mathcal{S}_t$ is valid[2] (according to Definition 2.1). Such constraints are presented in detail in [33] and summarized in this section. First, let the angles between centrelines of folds adjacent to a common interior fold intersection be denoted as α_{jk}, $j \in \{1, \ldots, N_{\mathcal{I}}\}$, $k \in \{1, \ldots, n_j\}$, where $N_{\mathcal{I}}$ is the number of fold intersections in the sheet and n_j is the number of folds adjacent to the jth interior fold intersection. A schematic illustrating these angles is provided in figure 3*a*. From figure 3, it is noted that fold intersections in origami with smooth folds correspond to holes in the sheet [33] while in conventional origami with creased folds the fold intersections correspond to single vertices [20,21]. Developability allows a surface to be flattened onto a plane without stretching or overlapping [38] and requires that the following constraint for the angles α_{jk} [39]:

$$2\pi - \sum_{k=1}^{n_j} \alpha_{jk} = 0. \tag{2.5}$$

The variables θ_{jk} and w_{jk}, $j \in \{1, \ldots, N_{\mathcal{I}}\}$, $k \in \{1, \ldots, n_j\}$, are those fold kinematic variables associated with the kth smooth fold adjacent to the jth interior fold intersection. These variables are obtained respectively from $\hat{\theta}_i$ and $\hat{w}_i$, $i \in \{1, \ldots, N_{\mathcal{F}}\}$, via a connectivity matrix (see [33] for details). Let $\boldsymbol{\gamma}_j(\eta) : [0, 1] \to \mathcal{S}_0$ be a simple closed path enclosing the jth interior fold intersection and crosses each smooth fold adjacent to the fold intersection once in counterclockwise order. An example of a path $\boldsymbol{\gamma}_j(\eta)$ is shown in figure 3*b*. The vectors $\mathbf{w}^{jk} \in \mathrm{span}(\mathbf{e}_1, \mathbf{e}_2)$ are those connecting the points where $\boldsymbol{\gamma}_j(\eta)$ enters and exits each smooth fold and $\mathbf{l}^{jk} \in \mathrm{span}(\mathbf{e}_1, \mathbf{e}_2)$ are those connecting the points where $\boldsymbol{\gamma}_j(\eta)$ enters and exits each face as shown in figure 3*b*.

Let $\mathbf{R}_i(\phi) \in \mathbb{R}^{3\times3}$ be the transformation matrix associated with a rotation by ϕ about an axis of rotation aligned to $\mathbf{e}_i$. For the initially closed strip of faces and smooth folds joined to the jth interior fold intersection to remain closed with each face undergoing a rigid deformation, the

[2]As stated in [33], self-intersection avoidance is not currently considered in the kinematic constraints presented for origami with smooth folds.

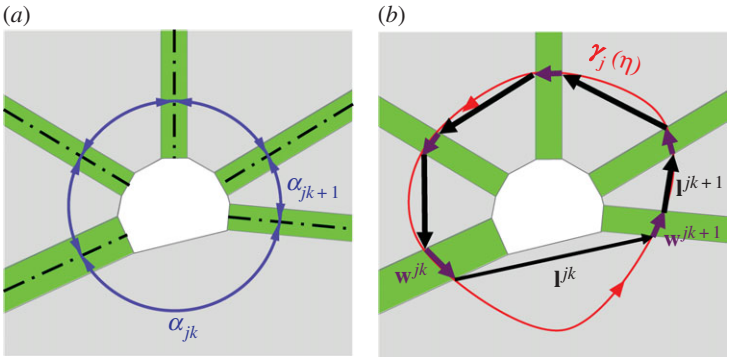

Figure 3. (*a*) Angles between centrelines of folds adjacent to a common interior fold intersection; (*b*) vectors $\mathbf{w}^{jk}$ and $\mathbf{l}^{jk}$ with start-points and endpoints corresponding to the points where the path $\boldsymbol{\gamma}_j(\eta)$ crosses the boundary rulings of the smooth folds. (Online version in colour.)

following constraints must hold[3]:

$$\mathbf{R}^j := \prod_{k=1}^{n_j} \mathbf{R}_1(\theta_{jk})\mathbf{R}_3(\alpha_{jk}) = \mathbf{I}_3, \tag{2.6}$$

which states that the rotation resulting from the ordered folds adjacent to the fold intersection is equal to the identity transformation, and

$$\mathbf{d}^j := \sum_{k=1}^{n_j} \left(\left(\prod_{l=1}^{k-1} \mathbf{R}_1(\theta_{jl})\mathbf{R}_3(\alpha_{jl}) \right) \left(\mathbf{R}_1\left(\frac{\theta_{jk}}{2}\right)\tilde{\mathbf{w}}^{jk} + \mathbf{R}_1(\theta_{jk})\tilde{\mathbf{l}}^{jk} \right) \right) = \mathbf{0}_3, \tag{2.7}$$

which states that the translation vector resulting from the ordered folds adjacent to such an intersection is equal to the zero vector. The vectors $\tilde{\mathbf{w}}^{jk}$ and $\tilde{\mathbf{l}}^{jk}$ correspond to the vectors $\mathbf{w}^{jk}$ and $\mathbf{l}^{jk}$ expressed in the coordinate system with the one-axis aligned with the fold centreline of the kth fold and the three-axis aligned with $\mathbf{e}_3$. Only such constraints are required given the assumed deformation of the smooth folds (only stretching and bending of their cross section). The centrelines of the smooth folds adjacent to a fold intersection do not have to intersect at a common point for such constraints to be applicable. The derivation for the constraints provided in equations (2.6) and (2.7) is presented in [33] and is not included here for the sake of brevity. For the special case of origami with creased folds, only the constraint in equation (2.6) is required to ensure valid configurations (refer to [33] for details).

(c) Kinematic simulation

The problem of kinematically simulating origami structures with smooth folds, which is fully addressed in [33], can be summarized as follows:

— Given: the geometric parameters that describe the fold pattern in a reference configuration $\mathcal{S}_0$ (vertex position vectors and fold widths, refer to figure 1*a*), and guess fold angle increments $\{{}^{IN}_{l}\Delta\hat{\boldsymbol{\theta}} \in \mathbb{R}^{N_{\mathcal{F}}} \mid l \in \{1, \ldots, n\}\}$,

— Find: the set of fold angles $\{\hat{\boldsymbol{\theta}}(t) \in \mathbb{R}^{N_{\mathcal{F}}} \mid t \in \{t_1, \ldots, t_n\}\}$ that satisfy the kinematic constraints presented in equations (2.6)–(2.7) closest to those resulting from the given fold angle increments, and the set of current configurations attained by the sheet $\{\mathcal{S}_t \mid t \in \{t_1, \ldots, t_n\}\}$.

[3]The identity matrix is denoted as $\mathbf{I}_n \in \mathbb{R}^{n\times n}$ and the zero vector is denoted as $\mathbf{0}_n \in \mathbb{R}^n$.

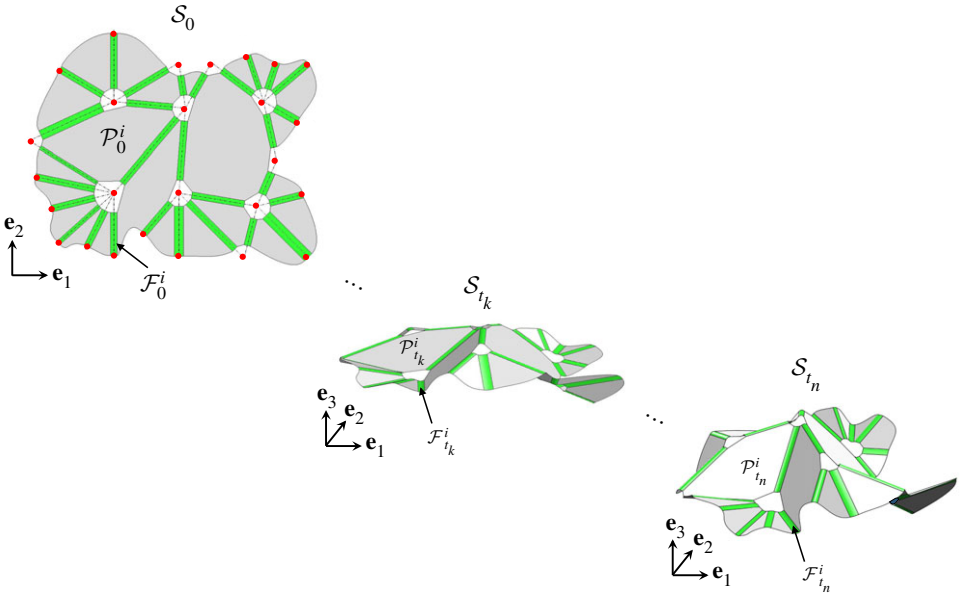

Figure 4. An origami sheet with smooth folds in its reference configuration $\mathcal{S}_0$, intermediate configuration $\mathcal{S}_{t_k}$, and final configuration $\mathcal{S}_{t_n}$. This result illustrates the capabilities of the kinematic simulation approach for origami structures with smooth folds presented in [33]. (Online version in colour.)

The numerical approach utilized to solve the aforementioned problem is presented in [33]. Figure 4 illustrates the capabilities of such a kinematic simulation approach for origami structures with smooth folds. The figure shows the reference configuration $\mathcal{S}_0$ and two current configurations $\mathcal{S}_{t_k}$ and $\mathcal{S}_{t_n}$ of a sheet having an arbitrary fold pattern subject to an arbitrary history of folding motion. This kinematic simulation approach is also adopted in this paper as described in the subsequent section and motivates the adopted approach to origami design.

3. Origami design problem description

As stated in §1, creating an origami structure having the desired characteristics, particularly a desired shape, is known as *origami design* [22]. Origami design is a challenge currently faced by designers and engineers who apply origami in various fields. This paper presents a novel method that aims to solve the following origami design problem:

— Given: a goal shape represented as a polygonal mesh (termed as the *goal mesh* $\mathcal{M}$),
— Find: the geometry of the reference configuration $\mathcal{S}_0$ of a single planar sheet, its pattern of smooth folds, and a history of folding motion from $\mathcal{S}_0$ to a folded configuration that approximates $\mathcal{M}$.

The method for origami design proposed in this paper is inspired from that provided by Tachi in [22,27] but allows for the consideration of smooth folds, as opposed to only creased folds addressed in [22,27]. As previously noted, a process for determining a history of folding motion $\mathcal{S}_0$ to a folded configuration that approximates $\mathcal{M}$ was not addressed in [22,27]. Therefore, the determination of such a history of folding motion represents another contribution of the present work and is applicable to both origami with smooth folds and conventional origami with creased folds. However, it is noted that when creased folds are considered, the interior fold intersections (that are holes in the sheet for the present method) may rather be filled with sheet regions containing specialized patterns of creased folds [22,27]. The folding deformation of such

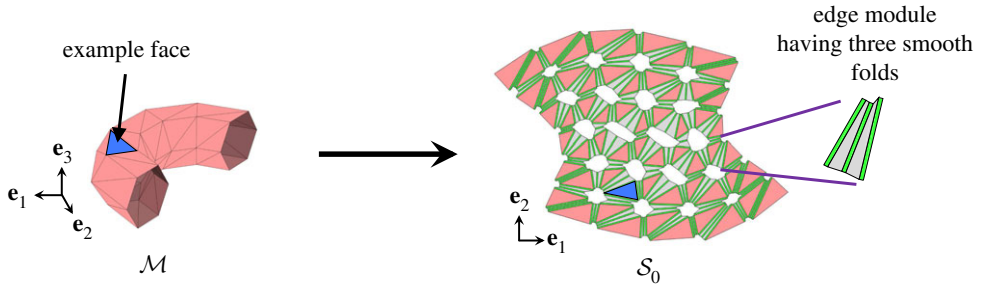

Figure 5. Schematic illustrating the method for origami design presented in this work: given a goal mesh $\mathcal{M}$, find the reference configuration $\mathcal{S}_0$ of a sheet that approximates $\mathcal{M}$ in a known folded configuration. The reference configuration $\mathcal{S}_0$ is comprised of the faces of $\mathcal{M}$ mapped to the plane spanned by $\mathbf{e}_1$ and $\mathbf{e}_2$ and introduced edge modules having two rigid faces and three smooth folds. (Online version in colour.)

regions is very complex as noted in [22] and therefore the present approach for determination of a history of folding motion (refer to §7) is not applicable in such a case. Nevertheless, if holes are included at the fold intersections as in the design method presented here, the proposed approach for determination of a history of folding motion can be applied to origami structures with smooth or creased folds.

The steps in the proposed method for origami design are the following:

(i) If the given polygonal mesh is not topologically equivalent to a disc [22], edge cuts introducing additional boundaries $\partial\mathcal{M}^C$ are applied (see section 2.2.1 of [22] for details and additional references regarding the mesh cut procedure). Further boundary edges forming $\partial\mathcal{M}^C$ can also be introduced as long as the resulting mesh satisfies the aforementioned topological property. A goal mesh $\mathcal{M}$ with boundary $\partial\mathcal{M} = \partial\mathcal{M}^C \cup \partial\mathcal{M}^O$ and faces $\mathcal{M}^j \subset \mathcal{M}$, $j \in \{1, \ldots, N_\mathcal{M}\}$ (where $N_\mathcal{M}$ is the total number of faces in $\mathcal{M}$) is then obtained. The boundary $\partial\mathcal{M}^O$ is comprised of the boundary edges of the originally given mesh. The goal mesh $\mathcal{M}$ is defined by its node position vectors $\{\hat{\mathbf{y}}^i \in \mathbb{R}^3 \mid i \in \{1, \ldots, N_\mathcal{N}\}\}$ (where $N_\mathcal{N}$ is the number of nodes in $\mathcal{M}$) and connectivity information describing which nodes are associated with each face $\mathcal{M}^j$ (refer to electronic supplementary material, section A.2 for details)

(ii) A planar sheet reference configuration $\mathcal{S}_0$ consisting of the faces $\mathcal{M}^j$, $j \in \{1, \ldots, N_\mathcal{M}\}$, mapped to the plane spanned by $\mathbf{e}_1$ and $\mathbf{e}_2$ and $N_\mathcal{E}^I$ introduced *edge modules* (where $N_\mathcal{E}^I$ is the number of interior edges of $\mathcal{M}$) is then determined (figure 5). The edge modules consist of *three smooth folds and two rigid faces* and are placed between every two faces of $\mathcal{M}$ connected by an interior edge[4], hence called edge modules. Thus, $\mathcal{S}_0$ has $3N_\mathcal{E}^I$ smooth folds and $2N_\mathcal{E}^I + N_\mathcal{M}$ rigid faces (refer to §2), i.e.

$$N_\mathcal{F} = 3N_\mathcal{E}^I, \quad N_\mathcal{P} = 2N_\mathcal{E}^I + N_\mathcal{M}. \tag{3.1}$$

Therefore, $\mathcal{S}_0 = (\bigcup_{i=1}^{3N_\mathcal{E}^I} \mathcal{F}_0^i) \cup (\bigcup_{i=1}^{2N_\mathcal{E}^I+N_\mathcal{M}} \mathcal{P}_0^i)$. The challenge in this step is to determine the geometry of the edge modules given the information of $\mathcal{M}$ and the fold widths of the smooth folds in each edge module (i.e. $\hat{w}_i^0$, $i \in \{1, \ldots, 3N_\mathcal{E}^I\}$) such that a valid reference configuration $\mathcal{S}_0$ is obtained (refer to §2) and such a sheet can approximate $\mathcal{M}$ in a known goal configuration $\mathcal{S}_\star$ ($\mathcal{S}_\star$ for the example shown in figure 5 is shown in figure 6)

(iii) The final step entails the determination of a history of folding motion from $\mathcal{S}_0$ to the goal configuration $\mathcal{S}_\star$. As described in §2c, the simulation of the motion of the sheet is performed in a sequence of increments. Thus, the challenge in this step is

[4]The idea of introducing such modules with three folds and to *tuck* fold them in order to approximate a three-dimensional goal shape was initially introduced for conventional origami with creased folds by Tachi in [22,27].

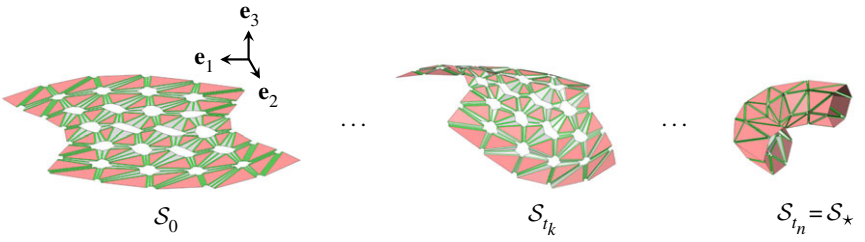

Figure 6. Folding motion of a determined sheet reference configuration $\mathcal{S}_0$ towards the goal configuration $\mathcal{S}_\star$ that approximates the goal mesh $\mathcal{M}$ (figure 5). (Online version in colour.)

the determination of the fold angle increments $\{{}^{IN}_{l}\Delta\hat{\boldsymbol{\theta}} \in \mathbb{R}^{3N^I_\mathcal{E}} \mid l \in \{1,\ldots,n\}\}$ leading to a set of fold angles $\{\hat{\boldsymbol{\theta}}(t) \in \mathbb{R}^{3N^I_\mathcal{E}} \mid t \in \{t_1,\ldots,t_n\}\}$ that results in the set of configurations $\{\mathcal{S}_t \mid t \in \{t_1,\ldots,t_n\}, \mathcal{S}_{t_n} = \mathcal{S}_\star\}$. Figure 6 shows configurations attained by the sheet from the example in figure 5 during a determined history of folding motion from $\mathcal{S}_0$ to $\mathcal{S}_\star$.

This work addresses (ii) and (iii) of the previous list (i.e. determination of $\mathcal{S}_0$ given $\mathcal{M}$ and fold widths $\hat{w}^0_i$, $i \in \{1,\ldots,3N^I_\mathcal{E}\}$, and subsequent determination of a history of folding motion from $\mathcal{S}_0$ to $\mathcal{S}_\star$). Algorithms to determine a boundary that yields a surface mesh topologically equivalent to a disc are available in the literature [22,40] and are not the subject of this work.

4. Design method

As described in §3, the design method proposed herein aims first to determine the geometry of a planar sheet configuration $\mathcal{S}_0$ and its pattern of smooth folds that approximates a given three-dimensional surface goal shape represented as a polygonal mesh $\mathcal{M}$ in a known configuration (denoted as the *goal configuration* $\mathcal{S}_\star$). The method is based on the previously known idea of using folds to create flaps that are *tucked* in order to morph an initially planar sheet towards an arbitrary three-dimensional shape [22,27].

The *goal mesh* $\mathcal{M}$ is a three-dimensional polygonal mesh topologically equivalent to a disc and having a boundary denoted as $\partial\mathcal{M}$. The polygonal faces forming $\mathcal{M}$ are denoted $\mathcal{M}^j$ such that $\mathcal{M} = \bigcup_{i=1}^{N_\mathcal{M}} \mathcal{M}^j$. The boundary of the originally given mesh is denoted $\partial\mathcal{M}^O$ (refer to figure 7). For a given mesh that is not topologically equivalent to a disc, interior edges of such a mesh are assigned as boundary edges forming a boundary $\partial\mathcal{M}^C$ in order to obtain a goal mesh $\mathcal{M}$ that has a single continuous boundary $\partial\mathcal{M} = \partial\mathcal{M}^C \cup \partial\mathcal{M}^O$ (see the example shown in figure 7). It is noted that the assignment of boundary edges forming $\partial\mathcal{M}^C$ may not only be used to generate a valid goal mesh $\mathcal{M}$ but also to obtain different sheet reference configurations for the given mesh. Criteria for determining an optimal boundary $\partial\mathcal{M}$ is not currently addressed but can be found in the literature [22,40].

An example of a simple goal mesh $\mathcal{M}$ is shown in figure 8. The goal mesh has $N_\mathcal{N}$ nodes and $N_\mathcal{E}$ edges ($N_\mathcal{N} = 25$ and $N_\mathcal{E} = 56$ for the goal mesh shown in figure 8). The number of interior nodes, i.e. those not contained in $\partial\mathcal{M}$, is denoted $N^I_\mathcal{N}$. As stated in the previous section, each node in $\mathcal{M}$ has an associated position vector $\hat{\mathbf{y}}^i \in \mathbb{R}^3$, $i \in \{1,\ldots,N_\mathcal{N}\}$[5]. Each polygonal face $\mathcal{M}^j$ is defined by its ordered associated nodes. Therefore, the *input data* required to define $\mathcal{M}$ is the following: (i) the node position vectors $\hat{\mathbf{y}}^i$, $i \in \{1,\ldots,N_\mathcal{N}\}$, and (ii) the index list of the nodes associated with each polygonal face $\mathcal{M}^j$ (in a counterclockwise ordering which is adopted in this work). The connectivity matrices obtained from this input data and the mappings among various parameters and variables used in this work are provided in electronic supplementary material, section A.

[5]A hat (ˆ) is used to distinguish the mesh-related geometric parameters and variables from those face- and node-related ones.

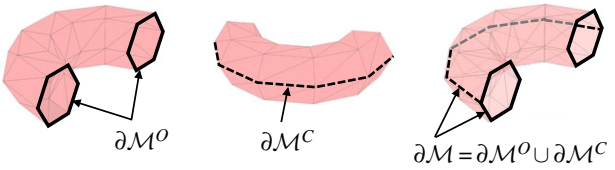

Figure 7. Outer edges of the given polygonal mesh forming the boundary $\partial\mathcal{M}^0$, additional boundary cut $\partial\mathcal{M}^C$, and the boundary of the *goal mesh* $\mathcal{M}$ denoted $\partial\mathcal{M} = \partial\mathcal{M}^C \cup \partial\mathcal{M}^0$. This figure is associated with the example shown in figure 5. (Online version in colour.)

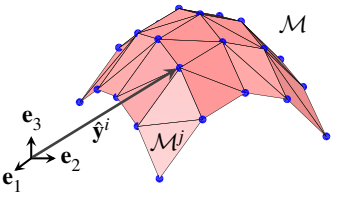

Figure 8. Schematic showing a goal mesh $\mathcal{M}$. A node position vector $\hat{\mathbf{y}}^i$ and a goal mesh face $\mathcal{M}^j$ are also shown. (Online version in colour.)

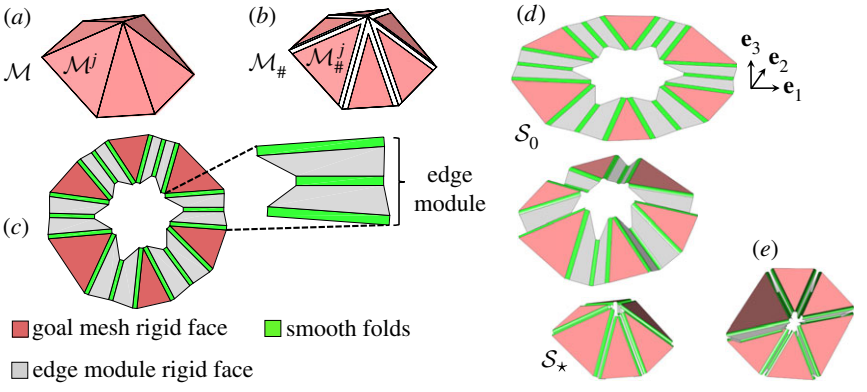

Figure 9. (*a*) Example goal mesh $\mathcal{M}$ having one interior node; (*b*) trimmed mesh $\mathcal{M}_\sharp$; (*c*) determined sheet geometry and fold pattern associated with the goal mesh shown in (*a*); (*d*) folding motion from the reference planar configuration $\mathcal{S}_0$ to the goal configuration $\mathcal{S}_\star$. Note that $\mathcal{M}_\sharp \subset \mathcal{S}_\star$ under appropriate rigid transformations; (*e*) view of the non-intersecting tucked edge modules in the goal configuration $\mathcal{S}_\star$. (Online version in colour.)

The steps towards determining a planar sheet having smooth folds that morphs towards the input goal mesh and its subsequent kinematic analysis are illustrated in figure 9. A simple example of a goal mesh $\mathcal{M}$ is presented in figure 9*a*. The faces $\mathcal{M}^j$ are initially trimmed to account for the gap that will be created by the tucked edge modules (figure 9*b*). The face trimming process is described in detail in §3a. The trimmed mesh is denoted as $\mathcal{M}_\sharp$ and its associated trimmed faces are denoted as $\mathcal{M}^j_\sharp$ such that $\mathcal{M}_\sharp = \bigcup_{i=1}^{N_\mathcal{M}} \mathcal{M}^j_\sharp$.

The method proceeds by determining the geometry of the *edge modules* (figure 9*c*) that are placed between any two trimmed faces $\mathcal{M}^j_\sharp$ and $\mathcal{M}^k_\sharp$ having associated goal mesh faces $\mathcal{M}^j$ and $\mathcal{M}^k$ joined by an interior edge. The *edge modules* are comprised of three smooth folds and

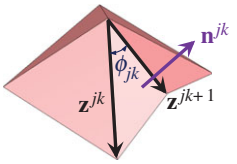

Figure 10. Geometric parameters associated with the faces of $\mathcal{M}$ having a common interior node. (Online version in colour.)

two rigid faces and are designed such that the faces $\mathcal{M}_\sharp^j$ together with these edge modules can be placed as a connected surface on the plane spanned by $\mathbf{e}_1$ and $\mathbf{e}_2$. Such a resulting planar surface corresponds to the sheet reference configuration $\mathcal{S}_0$ (figure 9*d*). A possible extension of the proposed design method could consider the replacement of certain edge modules by single smooth folds and thus allow for simplification of the determined sheet designs and reduction of the total number of folds. However, here the approach of [22,27] is taken where an edge module is applied for each interior edge of the goal mesh due to its wide applicability to a range of origami structural design problems. The aforementioned extension is strongly recommended for future studies.

During folding motion of the designed sheet, each edge module is tucked to morph the sheet towards its *goal configuration* $\mathcal{S}_\star$ for which the folds angles are known from the goal mesh data (figure 9*d*). Note that $\mathcal{M}_\sharp \subset \mathcal{S}_\star$ under appropriate rigid transformations. A view of the tucked edge modules, that are designed such that they do not intersect in the goal configuration, is shown in figure 9*e*.

Let $\mathbf{z}^{jk} \in \mathbb{R}^3, j \in \{1, \ldots, N_{\mathcal{N}}^I\}, k \in \{1, \ldots, n_j^{\mathcal{M}}\}$, be the vectors connecting the jth interior node to its kth adjacent node, defined in counterclockwise order, where $n_j^{\mathcal{M}}$ is the number of faces connected to the jth interior node (figure 10). These vectors are readily determined from the provided input data (see electronic supplementary material, section A.3). The parameters associated with the faces of $\mathcal{M}$ having a common interior node are the face angles ϕ_{jk} and the face unit normal vectors $\mathbf{n}^{jk} \in \mathbb{R}^3, j \in \{1, \ldots, N_{\mathcal{N}}^I\}, k \in \{1, \ldots, n_j^{\mathcal{M}}\}$. These parameters are determined respectively as follows:

$$\phi_{jk} = \cos^{-1}\left(\frac{\mathbf{z}^{jk} \cdot \mathbf{z}^{j\,k+1}}{\|\mathbf{z}^{jk}\|\,\|\mathbf{z}^{jk+1}\|}\right), \quad \mathbf{n}^{jk} = \frac{\mathbf{z}^{jk} \times \mathbf{z}^{jk+1}}{\|\mathbf{z}^{jk} \times \mathbf{z}^{jk+1}\|}. \tag{4.1}$$

(a) Face trimming

A side view of a tucked edge module is shown in figure 11. It is assumed that each edge module is tucked in a symmetric manner and therefore the exterior folds for each edge module (folds 1 and 3 in figure 11) have the same values for their geometric variables at $\mathcal{S}_\star$. The interior fold (fold 2 in figure 11) has a fold angle of π when the edge module is tucked at $\mathcal{S}_\star$. It is observed in figure 11 that due to the bending deformation of the smooth folds (as opposed to creasing), a gap results between two mesh faces connected to the edge module in the goal configuration $\mathcal{S}_\star$. To account for this gap, the faces of the goal mesh are initially recomputed to generate the *trimmed* mesh as shown in figure 9*b*. The removed regions compensate for the gaps and have an associated length $\hat{l}_i, i \in \{1, \ldots, N_{\mathcal{E}}^I\}$, as shown in figure 11. To define these removed regions, first the edge dihedral angle $\hat{\Theta}_i \in (0, 2\pi), i \in \{1, \ldots, N_{\mathcal{E}}^I\}$, is calculated as follows (figure 11):

$$\hat{\Theta}_i = \begin{cases} \pi + \cos^{-1}(\hat{\mathbf{n}}^{i1} \cdot \hat{\mathbf{n}}^{i2}); & \text{for convex edges} \\ \pi - \cos^{-1}(\hat{\mathbf{n}}^{i1} \cdot \hat{\mathbf{n}}^{i2}); & \text{for concave edges} \end{cases}, \tag{4.2}$$

where $\hat{\mathbf{n}}^{i1}$ and $\hat{\mathbf{n}}^{i2}$ are the unit normals of the faces adjacent to the ith interior edge.

Let $\hat{w}_i^{\text{I}\star}$ be the distance between the cross-section endpoints of the interior fold in the ith edge module at $\mathcal{S}_\star$, respectively (figure 11). Also, let $w_i^{\text{E}\star}$ be the distance between the cross-section

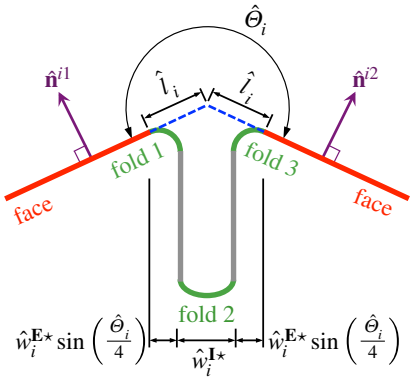

	fold with	fold angle at $\mathcal{S}_\star$	distance between cross-section endpoints at $\mathcal{S}_\star$
fold 1	$\hat{w}_i^{\mathrm{E}0}$	$-\hat{\Theta}_i/2$	$\hat{w}_i^{\mathrm{E}\star}$
fold 2	$\hat{w}_i^{\mathrm{I}0}$	π	$\hat{w}_i^{\mathrm{I}\star}$
fold 3	$\hat{w}_i^{\mathrm{E}0}$	$-\hat{\Theta}_i/2$	$\hat{w}_i^{\mathrm{E}\star}$

Figure 11. Side view of an example tucked edge module and its adjacent goal mesh faces at the goal configuration $\mathcal{S}_\star$. The geometric parameters defining the trim length $\hat{l}_i$ are shown. The fold width and kinematic variables of the smooth folds at the goal configuration $\mathcal{S}_\star$ are provided in the table on the right. (Online version in colour.)

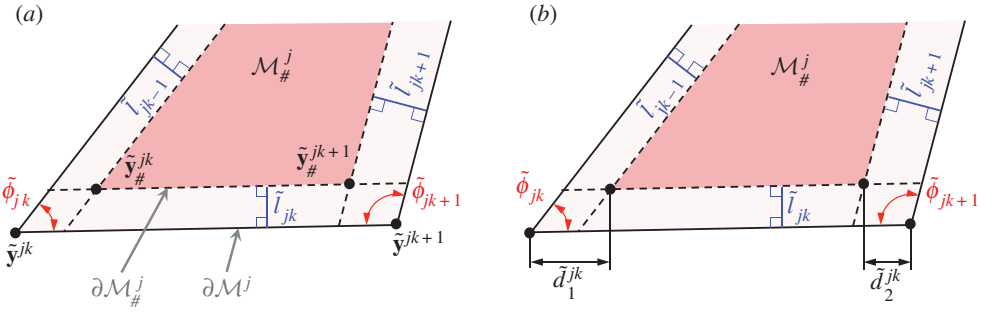

Figure 12. (*a*) Coordinates of the corner points of a face before and after trimming. The boundaries of $\mathcal{M}^j$ and $\mathcal{M}^j_\sharp$ are respectively denoted as $\partial\mathcal{M}^j$ and $\partial\mathcal{M}^j_\sharp$. (*b*) Parameters $\tilde{d}^{jk}_m$, $m = 1, 2$, associated with the change in length of each edge of $\mathcal{M}$ due to face trimming. (Online version in colour.)

endpoints of the exterior folds. The trim lengths $\hat{l}_i$ are then calculated as follows (refer to figure 11)

$$\hat{l}_i = \left(\frac{\hat{w}_i^{\mathrm{I}\star}}{2} + \hat{w}_i^{\mathrm{E}\star}\sin\left(\frac{\hat{\Theta}_i}{4}\right)\right)\csc\left(\frac{\hat{\Theta}_i}{2}\right). \tag{4.3}$$

Let n_j^C be the number of corners of the goal mesh polygonal face $\mathcal{M}^j$. Also, let $\tilde{\mathbf{y}}^{jk} \in \mathbb{R}^3$, $k \in \{1, \ldots, n_j^C\}$, be the position vectors of the nodes corresponding to the corners of $\mathcal{M}^j$, ordered counterclockwise.[6] The position vectors of the corner points of the trimmed face $\mathcal{M}^j_\sharp$, denoted $\tilde{\mathbf{y}}^{jk}_\sharp \in \mathbb{R}^3$, $k \in \{1, \ldots, n_j^C\}$, are determined as follows (refer to figure 12*a*):

$$\tilde{\mathbf{y}}^{jk}_\sharp = \tilde{\mathbf{y}}^{jk} + \tilde{l}_{jk-1}\csc(\tilde{\phi}_{jk})\frac{\tilde{\mathbf{y}}^{jk+1} - \tilde{\mathbf{y}}^{jk}}{\|\tilde{\mathbf{y}}^{jk+1} - \tilde{\mathbf{y}}^{jk}\|} + \tilde{l}_{jk}\csc(\tilde{\phi}_{jk})\frac{\tilde{\mathbf{y}}^{jk-1} - \tilde{\mathbf{y}}^{jk}}{\|\tilde{\mathbf{y}}^{jk-1} - \tilde{\mathbf{y}}^{jk}\|}, \tag{4.4}$$

[6] A tilde (˜) is used to distinguish the face-related parameters and variables from mesh- and node-related ones.

where the interior corner angles of $\mathcal{M}^j$ denoted as $\tilde{\phi}_{jk}$ are determined as follows:

$$\tilde{\phi}_{jk} = \cos^{-1}\left(\frac{(\tilde{\mathbf{y}}^{jk-1} - \tilde{\mathbf{y}}^{jk}) \cdot (\tilde{\mathbf{y}}^{jk+1} - \tilde{\mathbf{y}}^{jk})}{\|\tilde{\mathbf{y}}^{jk-1} - \tilde{\mathbf{y}}^{jk}\| \, \|\tilde{\mathbf{y}}^{jk+1} - \tilde{\mathbf{y}}^{jk}\|}\right), \tag{4.5}$$

and $\tilde{l}_{jk}$, $k \in \{1, \ldots, n_j^C\}$, is the trim length associated with the kth edge of $\mathcal{M}^j$. The mapping from the edge trim lengths $\hat{l}_i$, $i \in \{1, \ldots, N_{\mathcal{E}}^I\}$, to each set $\tilde{l}_{jk}$, $k \in \{1, \ldots, n_j^C\}$, is provided in electronic supplementary material, section A.2.

Only the length of the edges of $\mathcal{M}^j$ is altered by the face trimming process, while its corner angles remain unchanged under the condition stated in the following proposition:

Proposition 4.1. *The faces $\mathcal{M}^j$ and $\mathcal{M}_\sharp^j$ have equal corner angles if and only if $\mathcal{M}_\sharp^j$ is not a degenerate case of $\mathcal{M}^j$ and has the same orientation of $\mathcal{M}^j$.*

Proof. If $\mathcal{M}^j$ and $\mathcal{M}_\sharp^j$ have equal corner angles, then $\mathcal{M}_\sharp^j$ is not a degenerate case of $\mathcal{M}^j$ and both have the same orientation. To show sufficiency, it is first noted that if the vectors $\tilde{\mathbf{y}}_\sharp^{jk+1} - \tilde{\mathbf{y}}_\sharp^{jk}$ and $\tilde{\mathbf{y}}^{jk+1} - \tilde{\mathbf{y}}^{jk}$ have the same direction $\forall k \in \{1, \ldots, n_j^C\}$, the corner angles of $\mathcal{M}^j$ and $\mathcal{M}_\sharp^j$ are equal. The vector $\tilde{\mathbf{y}}_\sharp^{jk+1} - \tilde{\mathbf{y}}_\sharp^{jk}$ is decomposed as follows:

$$\tilde{\mathbf{y}}_\sharp^{jk+1} - \tilde{\mathbf{y}}_\sharp^{jk} = (\tilde{\mathbf{y}}_\sharp^{jk+1} - \tilde{\mathbf{y}}_\sharp^{jk})^{\parallel} + (\tilde{\mathbf{y}}_\sharp^{jk+1} - \tilde{\mathbf{y}}_\sharp^{jk})^{\perp}, \tag{4.6}$$

where $(\tilde{\mathbf{y}}_\sharp^{jk+1} - \tilde{\mathbf{y}}_\sharp^{jk})^{\parallel}$ and $(\tilde{\mathbf{y}}_\sharp^{jk+1} - \tilde{\mathbf{y}}_\sharp^{jk})^{\perp}$ are respectively parallel and orthogonal to $\tilde{\mathbf{y}}^{jk+1} - \tilde{\mathbf{y}}^{jk}$. The vector $(\tilde{\mathbf{y}}_\sharp^{jk+1} - \tilde{\mathbf{y}}_\sharp^{jk})^{\parallel}$ is given as follows:

$$\begin{aligned}(\tilde{\mathbf{y}}_\sharp^{jk+1} - \tilde{\mathbf{y}}_\sharp^{jk})^{\parallel} &= \frac{(\tilde{\mathbf{y}}_\sharp^{jk+1} - \tilde{\mathbf{y}}_\sharp^{jk}) \cdot (\tilde{\mathbf{y}}^{jk+1} - \tilde{\mathbf{y}}^{jk})}{\|\tilde{\mathbf{y}}^{jk+1} - \tilde{\mathbf{y}}^{jk}\|^2}(\tilde{\mathbf{y}}^{jk+1} - \tilde{\mathbf{y}}^{jk}),\\ &= \left(1 - \frac{\tilde{l}_{jk-1}\csc(\tilde{\phi}_{jk}) + \tilde{l}_{j\,k+1}\csc(\tilde{\phi}_{j\,k+1})}{\|\tilde{\mathbf{y}}^{j\,k+1} - \tilde{\mathbf{y}}^{jk}\|}\right.\\ &\quad \left. - \frac{\tilde{l}_{jk}(\cot(\tilde{\phi}_{jk}) + \cot(\tilde{\phi}_{jk+1}))}{\|\tilde{\mathbf{y}}^{jk+1} - \tilde{\mathbf{y}}^{jk}\|}\right)(\tilde{\mathbf{y}}^{jk+1} - \tilde{\mathbf{y}}^{jk}),\end{aligned} \tag{4.7}$$

and the square of the magnitude of the vector $(\tilde{\mathbf{y}}_\sharp^{jk+1} - \tilde{\mathbf{y}}_\sharp^{jk})^{\perp}$ is given as:

$$\begin{aligned}\|(\tilde{\mathbf{y}}_\sharp^{j\,k+1} - \tilde{\mathbf{y}}_\sharp^{jk})^{\perp}\|^2 &= \|(\tilde{\mathbf{y}}_\sharp^{j\,k+1} - \tilde{\mathbf{y}}_\sharp^{jk}) - (\tilde{\mathbf{y}}_\sharp^{j\,k+1} - \tilde{\mathbf{y}}_\sharp^{jk})^{\parallel}\|^2,\\ &= \tilde{l}_{jk}^2(\csc(\tilde{\phi}_{j\,k+1})^2 + \csc(\tilde{\phi}_{jk})^2 - (\cot(\tilde{\phi}_{jk}) + \cot(\tilde{\phi}_{j\,k+1}))^2\\ &\quad + 2\csc(\tilde{\phi}_{jk})\csc(\tilde{\phi}_{j\,k+1})\cos(\tilde{\phi}_{jk} + \tilde{\phi}_{j\,k+1})),\\ &= 0.\end{aligned} \tag{4.8}$$

Thus, $(\tilde{\mathbf{y}}_\sharp^{j\,k+1} - \tilde{\mathbf{y}}_\sharp^{jk}) = (\tilde{\mathbf{y}}_\sharp^{j\,k+1} - \tilde{\mathbf{y}}_\sharp^{jk})^{\parallel}$ which implies that $\tilde{\mathbf{y}}_\sharp^{j\,k+1} - \tilde{\mathbf{y}}_\sharp^{jk}$ is parallel to $\tilde{\mathbf{y}}^{j\,k+1} - \tilde{\mathbf{y}}^{jk}$. The coefficient of $(\tilde{\mathbf{y}}^{j\,k+1} - \tilde{\mathbf{y}}^{jk})$ in equation (4.7) must be positive[7] for the face $\mathcal{M}_\sharp^j$ to not be a degenerate case of $\mathcal{M}^j$ and also to have the same orientation of $\mathcal{M}^j$, which then implies that the faces $\mathcal{M}^j$ and $\mathcal{M}_\sharp^j$ have equal corner angles because the vectors $\tilde{\mathbf{y}}_\sharp^{j\,k+1} - \tilde{\mathbf{y}}_\sharp^{jk}$ and $\tilde{\mathbf{y}}^{j\,k+1} - \tilde{\mathbf{y}}^{jk}$ have the same direction. ∎

[7]This requirement is revisited in §6.

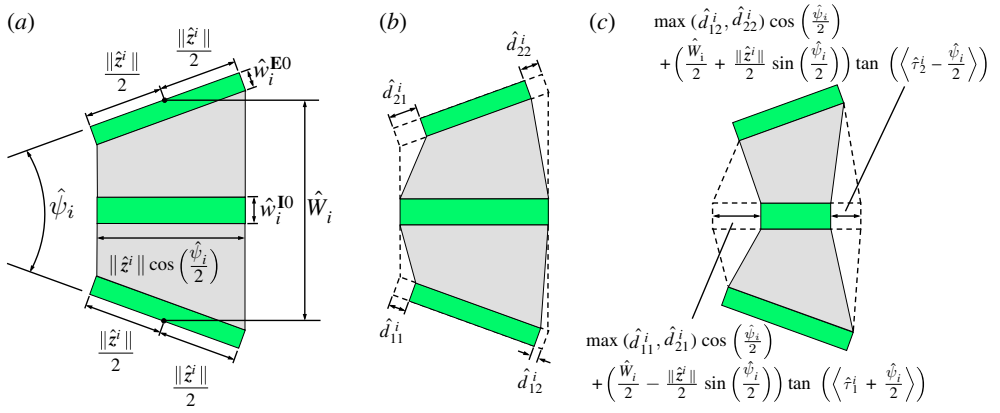

Figure 13. (*a*) Edge module and associated geometric parameters; (*b*) modified edge module accounting for the change in edge lengths due to face trimming; (*c*) edge module trimmed accounting for self-intersection avoidance at the goal configuration $\mathcal{S}_\star$ (addressed in electronic supplementary material, section B). (Online version in colour.)

The parameters $\tilde{d}_1^{jk}$ and $\tilde{d}_2^{jk}$ are associated with the change in length of the edges of $\mathcal{M}^j$ due to face trimming and are determined as follows (refer to figure 12*b*):

$$\tilde{d}_1^{jk} = \tilde{l}_{j\,k-1}\csc(\tilde{\phi}_{jk}) + \tilde{l}_{jk}\cot(\tilde{\phi}_{jk}), \quad \tilde{d}_2^{jk} = \tilde{l}_{j\,k+1}\csc(\tilde{\phi}_{j\,k+1}) + \tilde{l}_{jk}\cot(\tilde{\phi}_{j\,k+1}). \tag{4.9}$$

(b) Design parametrization and constraints

As all fold widths are assumed given (refer to §3), the fold widths of the interior and exterior folds of each edge module in the planar reference configuration $\mathcal{S}_0$, respectively, denoted as $\hat{w}_i^{\mathrm{I}0}$ and $\hat{w}_i^{\mathrm{E}0}$, are inputs to the design problem (figure 13*a*). In practice, the fold widths $\hat{w}_i^{\mathrm{I}0}$ and $\hat{w}_i^{\mathrm{E}0}$, $i \in \{1, \ldots, N_{\mathcal{E}}^I\}$, are determined such that the smooth folds comprised of a specific material are able to achieve their required fold angles at $\mathcal{S}_\star$ (figure 11). Such a physically-based determination of the fold widths is a topic of future work.

In addition to the information regarding fold widths, each edge module in the designed sheet is parametrized by two variables corresponding to $\hat{W}_i$ and $\hat{\psi}_i$. These variables are schematically shown in figure 13*a*. The modified edge module accounting for the change in edge lengths due to face trimming (refer to §3a) is presented in figure 13*b*. The parameters $\hat{d}_{nm}^i$, $n, m \in \{1, 2\}$, shown therein correspond to those parameters $\tilde{d}_m^{jk}$, $m \in \{1, 2\}$ (see equation (4.9)), of the two faces connected to the ith interior edge (refer to electronic supplementary material, section A.3 for the mapping among such sets of variables).

Let W_{jk} and ψ_{jk}, $j \in \{1, \ldots, N_{\mathcal{N}}^I\}$, $k \in \{1, \ldots, n_j^{\mathcal{M}}\}$, be the variables $\hat{W}_i$ and $\hat{\psi}_i$, respectively, of the edge module associated with the kth interior edge adjacent to the jth interior node of $\mathcal{M}$. The mapping from the sets of all the edge module variables $\hat{W}_i$ and $\hat{\psi}_i$, $i \in \{1, \ldots, N_{\mathcal{E}}^I\}$, to the sets W_{jk} and ψ_{jk}, $j \in \{1, \ldots, N_{\mathcal{N}}^I\}$, $k \in \{1, \ldots, n_j^{\mathcal{M}}\}$, is provided in electronic supplementary material, section A.3. The variables W_{jk} and ψ_{jk}, $k \in \{1, \ldots, n_j^{\mathcal{M}}\}$ must be determined such that the faces of $\mathcal{M}_\sharp$ and the edge modules associated with the jth interior node of $\mathcal{M}$ form a closed strip in $\mathcal{S}_0$. If this requirement is met, where a pair of faces in $\mathcal{M}$ is connected by an interior edge, their associated faces in $\mathcal{M}_\sharp$ are connected in $\mathcal{S}_0$ by an edge module. Such a requirement is associated with the following constraints:

Proposition 4.2. *For the faces of $\mathcal{M}_\sharp$ and the edge modules associated with the jth interior node of $\mathcal{M}$ to form a closed strip in $\mathcal{S}_0$, the following constraints must hold*:

$$2\pi = \sum_{k=1}^{n_j^{\mathcal{M}}} \phi_{jk} + \sum_{k=1}^{n_j^{\mathcal{M}}} \psi_{jk}, \tag{4.10}$$

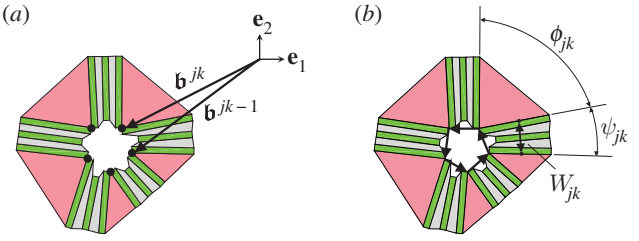

Figure 14. Sub-domain of $\mathcal{S}_0$ associated with the jth interior node of $\mathcal{M}$: (*a*) position vectors of the edge module corner points, (*b*) face corner and edge module angles. (Online version in colour.)

and:

$$\mathbf{0}_3 = \sum_{k=1}^{n_j^{\mathcal{M}}} \left(\mathbf{R}_3 \left(\sum_{l=1}^{k-1} \left(\frac{\psi_{jl}}{2} + \phi_{jl} + \frac{\psi_{jl+1}}{2} \right) \right) \begin{bmatrix} (d_{21}^{jk} - d_{11}^{jk}) \cos\left(\frac{\psi_{jk}}{2}\right) \\ W_{jk} + (d_{11}^{jk} + d_{21}^{jk} - \|\mathbf{z}^{jk}\|) \sin\left(\frac{\psi_{jk}}{2}\right) \\ 0 \end{bmatrix} \right). \tag{4.11}$$

Proof. Let $\mathfrak{b}^{jk} \in \mathrm{span}(\mathbf{e}_1, \mathbf{e}_2)$, $k \in \{0, \ldots, n_j^{\mathcal{M}}\}$, be the corner position vectors of the edge modules associated with the jth interior node of $\mathcal{M}$ at the reference configuration $\mathcal{S}_0$ (figure 14). The position vectors of two of the corners of the kth edge module correspond to $\mathfrak{b}^{jk-1}$ and $\mathfrak{b}^{jk}$. These position vectors can be determined recursively as follows (refer to figure 13*b*):

$$\begin{aligned} \mathfrak{b}^{jk} &= \mathfrak{b}^{jk-1} + \mathbf{R}_3 \left(\sum_{l=1}^{k-1} \left(\frac{\psi_{jl}}{2} + \phi_{jl} + \frac{\psi_{jl+1}}{2} \right) \right) \begin{bmatrix} (d_{21}^{jk} - d_{11}^{jk}) \cos\left(\frac{\psi_{jk}}{2}\right) \\ W_{jk} + (d_{11}^{jk} + d_{21}^{jk} - \|\mathbf{z}^{jk}\|) \sin\left(\frac{\psi_{jk}}{2}\right) \\ 0 \end{bmatrix}, \\ &= \sum_{l=1}^{k} \left(\mathbf{R}_3 \left(\sum_{m=1}^{l-1} \left(\frac{\psi_{jm}}{2} + \phi_{jm} + \frac{\psi_{jm+1}}{2} \right) \right) \begin{bmatrix} (d_{21}^{jl} - d_{11}^{jl}) \cos\left(\frac{\psi_{jl}}{2}\right) \\ W_{jl} + (d_{11}^{jl} + d_{21}^{jl} - \|\mathbf{z}^{jl}\|) \sin\left(\frac{\psi_{jl}}{2}\right) \\ 0 \end{bmatrix} \right) \\ &\quad + \mathfrak{b}^{j0}. \end{aligned} \tag{4.12}$$

Also define $\mathbf{Q}_3(\phi), \mathbf{T}(\mathbf{b}) \in \mathbb{R}^{4\times 4}$ as the matrices in homogeneous coordinates associated with a rotation by ϕ about $\mathbf{e}_3$ and a translation by $\mathbf{b} \in \mathbb{R}^3$, respectively

$$\mathbf{Q}_3(\phi) := \begin{bmatrix} \mathbf{R}_3(\phi) & \mathbf{0}_3 \\ \mathbf{0}_3^\top & 1 \end{bmatrix}, \quad \mathbf{T}(\mathbf{b}) := \begin{bmatrix} \mathbf{I}_3 & \mathbf{b} \\ \mathbf{0}_3^\top & 1 \end{bmatrix}. \tag{4.13}$$

Consider the transport of a position vector from the face with corner angle ϕ_{jk-1} to the face with corner angle ϕ_{jk}. The transformation associated with crossing the edge module located between these two faces can be decomposed into a translation by $\mathfrak{b}^{jk} - \mathfrak{b}^{jk-1}$ followed by a rotation of $\phi_{jk} + \psi_{jk}$ about an axis aligned to $\mathbf{e}_3$ and crossing the point with position vector $\mathfrak{b}^{jk}$. Such a transformation can be expressed in homogeneous coordinates as follows:

$$\mathbf{T}(\mathfrak{b}^{jk})\mathbf{Q}_3(\phi_{jk} + \psi_{jk})\mathbf{T}^{-1}(\mathfrak{b}^{jk})\mathbf{T}(\mathfrak{b}^{jk} - \mathfrak{b}^{jk-1}) = \mathbf{T}(\mathfrak{b}^{jk})\mathbf{Q}_3(\phi_{jk} + \psi_{jk})\mathbf{T}^{-1}(\mathfrak{b}^{jk-1}). \tag{4.14}$$

It follows that the composition of transformations presented in equation (4.14) associated with crossing the edge modules with angles ψ_{jk}, $k \in \{1, \ldots, n_j^{\mathcal{M}}\}$, must be identity transformation for these surfaces, along with the faces with corner angles ϕ_{jk}, $k \in \{1, \ldots, n_j^{\mathcal{M}}\}$, to form a closed strip

$$\mathbf{I}_4 = \prod_{k=1}^{n_j^{\mathcal{M}}} \mathbf{T}(\mathfrak{b}^{jk}) \mathbf{Q}_3(\phi_{jk} + \psi_{jk}) \mathbf{T}^{-1}(\mathfrak{b}^{j\,k-1}) = \mathbf{T}(\mathfrak{b}^{jn_j^{\mathcal{M}}}) \mathbf{Q}_3 \left(\sum_{k=1}^{n_j^{\mathcal{M}}} (\phi_{jk} + \psi_{jk}) \right) \mathbf{T}^{-1}(\mathfrak{b}^{j0}). \tag{4.15}$$

The equation above holds if $\sum_{k=1}^{n_j^{\mathcal{M}}} (\phi_{jk} + \psi_{jk}) = 2\pi n$ with $n \in \mathbb{Z}$. Specifically, n must be equal to 1 for the closed strip to be developable [38,41] yielding the constraint of equation (4.10). In addition to such a constraint, it is required that $\mathfrak{b}^{jn_j^{\mathcal{M}}} = \mathfrak{b}^{j0}$ for equation (4.15) to hold. Considering equation (4.12), $\mathfrak{b}^{jn_j^{\mathcal{M}}} = \mathfrak{b}^{j0}$ implies the constraint in equation (4.11). ■

Equation (4.11) implies that the addition of the vectors shown in figure 14 must be equal to $\mathbf{0}_3$. This equation provides two scalar constraints because the third component of such a vector equation is always equal to 0. Therefore, equations (4.10) and (4.11) provide a total of $3N_{\mathcal{N}}^I$ equality constraints.

In addition to the loop closure constraints provided in Proposition 4.2, other constraints must be imposed to ensure that the geometry of each individual edge module is valid. For instance, the interior fold (having fold width $\hat{w}_i^{\mathrm{I}0}$, see figure 13*a*) and the faces of an edge module degenerate to straight line segments if $\hat{\psi}_i$ reaches $\pm\pi$ (refer to figure 13*a*). Therefore, the following bounds must be imposed for this variable:

$$-\pi < \hat{\psi}_i < \pi. \tag{4.16}$$

Furthermore, the exterior folds (each having fold width $\hat{w}_i^{\mathrm{E}0}$, see figure 13*a*) of an edge module must not overlap with the interior fold. This requirement yields the following constraint (refer to figure 13*a*–*b*):

$$\hat{W}_i \geq \hat{w}_i^{\mathrm{I}0} + 2\hat{w}_i^{\mathrm{E}0} \cos\left(\frac{\hat{\psi}_i}{2}\right) + \|\hat{\mathbf{z}}^i\| \sin\left(\left|\frac{\hat{\psi}_i}{2}\right|\right) - \begin{cases} (\hat{d}_{11}^i + \hat{d}_{21}^i) \sin\left(\dfrac{\hat{\psi}_i}{2}\right); & \hat{\psi}_i \geq 0 \\ (\hat{d}_{12}^i + \hat{d}_{22}^i) \sin\left(-\dfrac{\hat{\psi}_i}{2}\right); & \hat{\psi}_i < 0 \end{cases}. \tag{4.17}$$

Equation (4.17) and the upper and lower bounds of $\hat{\psi}_i$ in equation (4.16) provide $3N_{\mathcal{E}}^I$ inequality constraints.

Intersections are not allowed in valid configurations (cf. Definition 2.1) and must be avoided when adjacent edge modules are tucked in the goal configuration $\mathcal{S}_\star$. To preclude such intersections in $\mathcal{S}_\star$, certain regions of the edge modules are removed (figure 13*c*) such that each edge module does not intersect any of its neighbouring edge modules. Such a process is denoted as *edge module trimming* and is summarized in electronic supplementary material, section B. Figure 15 shows the importance of the edge module trimming process. If the edge module trimming process is not considered and the edge module geometry is as given in figure 13*b*, adjacent edge modules intersect at the goal configuration $\mathcal{S}_\star$ as observed in figure 15*d*. However, if the edge module trimming process is considered and the geometry of the edge modules is as illustrated in figure 13*c*, no intersections among adjacent edge modules occur as shown in figure 15*g*. The angles $\hat{\tau}_1^i$ and $\hat{\tau}_2^i$, $i \in \{1, \ldots, N_{\mathcal{E}}^I\}$, are introduced to determine the trimmed regions the ith edge module as shown in figure 13*c*. These angles are obtained from their corresponding values in the set of angles τ_{jk}, $j \in \{1, \ldots, N_{\mathcal{N}}^I\}$, $k \in \{1, \ldots, n_j^{\mathcal{M}}\}$ (determined using the approach presented in electronic supplementary material, section B).

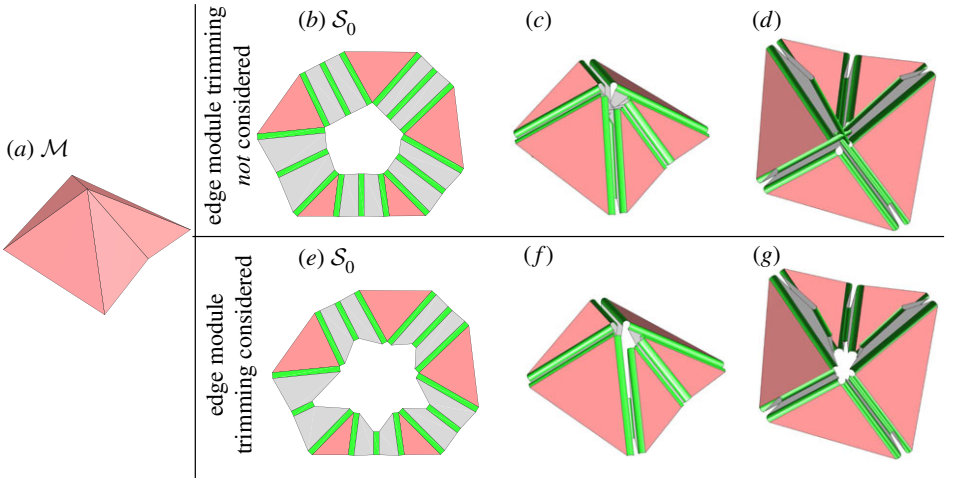

Figure 15. Example showing the need for *edge module trimming*. (*a*) A simple goal mesh $\mathcal{M}$. (*b*) and (*e*) Determined sheet reference configurations $\mathcal{S}_0$. Edge module trimming is not considered for the sheet reference configuration shown in (*b*) while such a process is considered for the reference configuration in (*e*). (*c–d*), (*f–g*) Exterior and interior views of the goal configuration $\mathcal{S}_\star$ for both cases. It is observed in (*d*) that if the edge module trimming process described in electronic supplementary material, section B is not considered, the tucked edge modules intersect at $\mathcal{S}_\star$. If such a process is considered, adjacent edge modules do not intersect in $\mathcal{S}_\star$ as shown in (*g*). (Online version in colour.)

Each edge module must remain connected after edge trimming. This requirement is satisfied if the following inequality holds for each edge module (refer to figure 13*c*)[8]:

$$\begin{aligned}\|\hat{\boldsymbol{z}}^i\| \cos\left(\frac{\hat{\psi}_i}{2}\right) > &\left(\frac{\hat{W}_i}{2} - \frac{\|\hat{\boldsymbol{z}}^i\|}{2}\sin\left(\frac{\hat{\psi}_i}{2}\right)\right)\tan\left(\left\langle \hat{\tau}_1^i + \frac{\hat{\psi}_i}{2}\right\rangle\right)\\ &+\left(\frac{\hat{W}_i}{2} + \frac{\|\hat{\boldsymbol{z}}^i\|}{2}\sin\left(\frac{\hat{\psi}_i}{2}\right)\right)\tan\left(\left\langle \hat{\tau}_2^i - \frac{\hat{\psi}_i}{2}\right\rangle\right)\\ &+(\max(\hat{d}_{11}^i, \hat{d}_{21}^i) + \max(\hat{d}_{12}^i, \hat{d}_{22}^i))\cos\left(\frac{\hat{\psi}_i}{2}\right).\end{aligned} \tag{4.18}$$

It is noted that if $(\hat{\tau}_1^i + \hat{\psi}_i/2) < 0$ or $(\hat{\tau}_2^i - \hat{\psi}_i/2) < 0$, these angles are set to 0 to prevent any increase in area of the edge modules during this process. Equation (4.18) yields the following constraint:

$$\begin{aligned}\hat{W}_i < &\frac{2(\|\hat{\boldsymbol{z}}^i\| - \max(\hat{d}_{11}^i, \hat{d}_{21}^i) - \max(\hat{d}_{12}^i, \hat{d}_{22}^i))\cos(\hat{\psi}_i/2)}{\tan(\langle\hat{\tau}_1^i + \hat{\psi}_i/2\rangle) + \tan(\langle\hat{\tau}_2^i - \hat{\psi}_i/2\rangle)}\\ &+\frac{\|\hat{\boldsymbol{z}}^i\|\sin(\hat{\psi}_i/2)(\tan(\langle\hat{\tau}_1^i + \hat{\psi}_i/2\rangle) - \tan(\langle\hat{\tau}_2^i - \hat{\psi}_i/2\rangle))}{\tan(\langle\hat{\tau}_1^i + \hat{\psi}_i/2\rangle) + \tan(\langle\hat{\tau}_2^i - \hat{\psi}_i/2\rangle)}.\end{aligned} \tag{4.19}$$

The preceding equation provides $N_{\mathcal{E}}^I$ additional inequality constraints. In summary, the proposed design method introduces $2N_{\mathcal{E}}^I$ design variables corresponding to $\hat{W}_i$ and $\hat{\psi}_i$, $i \in \{1, \ldots, N_{\mathcal{E}}^I\}$. The loop closure constraints (equations (4.10) and (4.11)) provide $3N_{\mathcal{N}}^I$ equality constraints. Equations (4.16), (4.17) and (4.19) allowing for valid edge module geometries and self-intersection avoidance in $\mathcal{S}_\star$ provide $4N_{\mathcal{E}}^I$ inequality constraints. The subsequent section describes the numerical implementation procedure used to determine a set of design variables that satisfies the aforementioned equality and inequality constraints.

[8]The Macaulay brackets are denoted as $\langle\cdot\rangle$ and defined as: $\langle y\rangle = \begin{cases} y; & y \geq 0 \\ 0; & y < 0 \end{cases}$.

Table 1. Numerical procedure used to determine a set of design variables that satisfies the constraints of the proposed design method.

1:	Set $l \leftarrow 1$ and provide initial guess ${}^{1}\mathbf{D}$
2:	Determine $\|\mathfrak{R}({}^{l}\mathbf{D})\|$
3:	IF $\|\mathfrak{R}({}^{l}\mathbf{D})\|/(3N^{l}_{\mathcal{N}} + 4N^{l}_{\mathcal{E}}) <$ tol THEN RETURN ${}^{l}\mathbf{D}$ and EXIT ELSE CONTINUE
4:	Determine ${}^{l+1}\mathbf{D}$ using equation (5.3)
5:	Set $l \leftarrow l + 1$ and GOTO 2

5. Numerical implementation

Given the goal mesh $\mathcal{M}$, the node coordinates of $\mathcal{M}$ and the mesh connectivity data (see electronic supplementary material, section A) are utilized to compute all the geometric parameters presented in the preceding section. Subsequently, the iterative numerical procedure presented in this section is used to determine a set of design variables $\hat{W}_i$ and $\hat{\psi}_i$, $i \in \{1, \ldots, N^{I}_{\mathcal{E}}\}$, that satisfies the proposed constraints. The vectors $\hat{\boldsymbol{W}} \in \mathbb{R}^{N^{I}_{\mathcal{E}}}$, $\hat{\boldsymbol{\psi}} \in \mathbb{R}^{N^{I}_{\mathcal{E}}}$ and $\mathbf{D} \in \mathbb{R}^{2N^{I}_{\mathcal{E}}}$ are defined as follows:

$$\hat{\boldsymbol{W}} := [\hat{W}_1 \quad \ldots \quad \hat{W}_{N^{I}_{\mathcal{E}}}]^{\top}, \quad \hat{\boldsymbol{\psi}} := [\hat{\psi}_1 \quad \ldots \quad \hat{\psi}_{N^{I}_{\mathcal{E}}}]^{\top}, \quad \mathbf{D} := [\hat{\boldsymbol{W}}^{\top} \quad \hat{\boldsymbol{\psi}}^{\top}]^{\top}. \tag{5.1}$$

The equality constraints (equations (4.10) and (4.11)) are set to the form $\boldsymbol{h} = \mathbf{0}_{3N^{I}_{\mathcal{N}}}$ while the inequality constraints (equations (4.16), (4.17) and (4.19)) are set to the form $\boldsymbol{g} \leq \mathbf{0}_{4N^{I}_{\mathcal{E}}}$[9]. Let $\mathfrak{R} \in \mathbb{R}^{3N^{I}_{\mathcal{N}}+4N^{I}_{\mathcal{E}}}$ be the residual vector defined as follows:

$$\mathfrak{R}(\mathbf{D}) := [\boldsymbol{h}(\mathbf{D})^{\top} \quad \max(\mathbf{0}_{4N^{I}_{\mathcal{E}}}, \boldsymbol{g}(\mathbf{D}))^{\top}]^{\top}, \tag{5.2}$$

where the $\max(\cdot,\cdot)$ operator in the previous equation is applied component-wise. At the lth iteration, if $\|\mathfrak{R}({}^{l}\mathbf{D})\|/(3N^{I}_{\mathcal{N}} + 4N^{I}_{\mathcal{E}}) \geq$ tol (where tol is a numerical tolerance), the design variables are corrected using the generalized Newton's method as follows:

$${}^{l}\Delta\mathbf{D} = -\left(\frac{\partial \mathfrak{R}({}^{l}\mathbf{D})}{\partial \mathbf{D}}\right)^{\dagger} \mathfrak{R}({}^{l}\mathbf{D}), \quad {}^{l+1}\mathbf{D} = {}^{l}\mathbf{D} + {}^{l}\Delta\mathbf{D}, \tag{5.3}$$

where $(\cdot)^{\dagger}$ denotes the Moore–Penrose pseudoinverse. Given an initial guess for ${}^{1}\mathbf{D}$, the design variables are iteratively updated as indicated in equation (5.3) until $\|\mathfrak{R}({}^{l}\mathbf{D})\|/(3N^{I}_{\mathcal{N}} + 4N^{I}_{\mathcal{E}}) <$ tol. Table 1 summarizes the procedure used to determine a set of design variables that satisfies the constraints of the proposed design method.

6. Discussion

A discussion of the requirements for the existence of determined sheet reference configurations is presented in this section. Uniqueness of determined sheet reference configurations is also discussed.

For the present design method to be applicable to a given goal mesh $\mathcal{M}$, it must be an *orientable manifold mesh*. The goal mesh $\mathcal{M}$ must be a manifold mesh because in the present design method each edge in $\mathcal{M}$ is assumed to be located either at $\partial\mathcal{M}$ or connecting two faces of $\mathcal{M}$. Orientability of $\mathcal{M}$ is also required because the faces of $\mathcal{M}_{\sharp}$, that have the same orientation as those of $\mathcal{M}$ (see Proposition 4.1), are mapped into a common plane in $\mathcal{S}_0$. As $\mathcal{S}_0$ is orientable, $\mathcal{M}$ must also have this property.

The face trimming process described in §3a must not degenerate any face of $\mathcal{M}$. This is clearly required because every face $\mathcal{M}^{j}$ and its associated trimmed face $\mathcal{M}^{j}_{\sharp}$ must have the same number

[9]For numerical implementation, strict inequality constraints $A < 0$ in equations (4.16) and (4.19) are expressed as non-strict inequalities of the form $A + \epsilon \leq 0$, where $\epsilon > 0$.

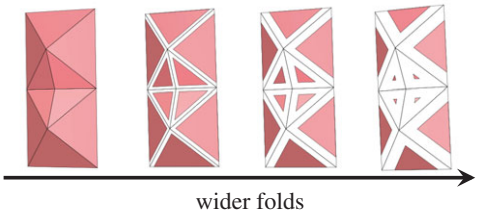

Figure 16. Trimmed faces associated with edge modules having smooth folds of various fold widths. The leftmost mesh corresponds to the special case of creased folds for which face trimming is not required. (Online version in colour.)

of edges. The following corollary of Proposition 4.1 provides a practical way to check if such a requirement is met:

Corollary 6.1. *The face trimming process does not degenerate any face $\mathcal{M}^j$ if and only if the following conditions hold*:

$$\left.\begin{aligned} &(\tilde{\boldsymbol{y}}^{jk+1} - \tilde{\boldsymbol{y}}^{jk}) \cdot (\tilde{\boldsymbol{y}}_\sharp^{jk+1} - \tilde{\boldsymbol{y}}_\sharp^{jk}) > 0 \;\Leftrightarrow\; \|\tilde{\boldsymbol{y}}^{jk+1} - \tilde{\boldsymbol{y}}^{jk}\| - \tilde{d}_1^{jk} - \tilde{d}_2^{jk} > 0 \\ \textit{and} \qquad &\forall j \in \{1, \ldots, N_{\mathcal{M}}\}, \quad k \in \{1, \ldots, n_j^C\}. \end{aligned}\right\} \tag{6.1}$$

The expressions for $\tilde{d}_1^{jk}$ and $\tilde{d}_2^{jk}$ are provided in equation (4.9). The size of the trimmed regions increases proportionally to the width of the folds as indicated in equation (4.3). The increase of the size of the trimmed regions with increase in fold widths is illustrated in figure 16. For the special case of creased folds that have zero fold width, face trimming is not required and such a requirement is trivially satisfied (see the leftmost schematic in figure 16). For any other case where the width of the folds is non-zero, the size of the goal mesh is subject to the following constraint:

$$\min_{j \in \{1,\ldots,N_{\mathcal{M}}\},\, k \in \{1,\ldots,n_j^C\}} \|\tilde{\mathbf{y}}^{jk+1} - \tilde{\mathbf{y}}^{jk}\| - \tilde{d}_1^{jk} - \tilde{d}_2^{jk} > 0. \tag{6.2}$$

A solution to the equality constraints (equations (4.10) and (4.11)) must be contained within the bounds of the design variables (equations (4.16), (4.17) and (4.19)). The necessity for such a requirement is evident. The number of degrees of freedom ($N_{\text{d.f.}}$) in the design problem is given as follows:

$$N_{\text{d.f.}} = 2N_{\mathcal{E}}^I - 3N_{\mathcal{N}}^I, \tag{6.3}$$

where $2N_{\mathcal{E}}^I$ is the number of design variables $\hat{W}_i$, $\hat{\psi}_i$, $i \in \{1, \ldots, N_{\mathcal{E}}^I\}$, and $3N_{\mathcal{N}}^I$ is the number of equality constraints. It is assumed in equation (6.3) that there are no redundant equality constraints and that the inequality constraints in equations (4.16), (4.17) and (4.19) permit solutions to the system of equations (4.10) and (4.11). The number of interior edges $N_{\mathcal{E}}^I$ is additively decomposed as follows:

$$N_{\mathcal{E}}^I = N_{\mathcal{E}}^{I0} + N_{\mathcal{E}}^{I1} + N_{\mathcal{E}}^{I2}, \tag{6.4}$$

where $N_{\mathcal{E}}^{Im}$, $m \in \{0, 1, 2\}$, is the number of interior edges connected to m interior nodes. Also consider the following equality:

$$\bar{n}^{\mathcal{M}} N_{\mathcal{N}}^I = \sum_{j=1}^{N_{\mathcal{N}}^I} n_j^{\mathcal{M}} = 2N_{\mathcal{E}}^{I2} + N_{\mathcal{E}}^{I1}, \tag{6.5}$$

where $\bar{n}^{\mathcal{M}}$ is the average valence of the interior nodes in $\mathcal{M}$ (i.e. the average number of edges incident to the each interior node). Substituting equations (6.4) and (6.5) into equation (6.3), the

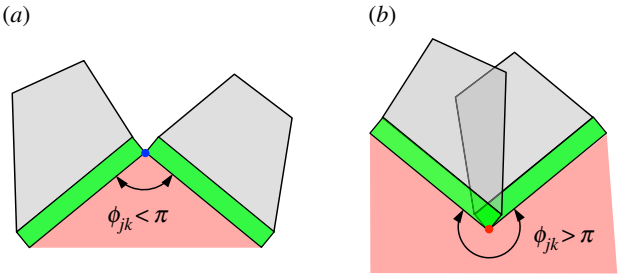

Figure 17. (*a*) Edge modules connected to a face with a convex face angle. (*b*) Edge modules connected to a face with a concave face angle. (Online version in colour.)

following relation between d.f. and number of interior edges is obtained:

$$N_{\text{d.f.}} = \left(2 - \frac{6}{\bar{n}^{\mathcal{M}}}\right) N_{\mathcal{E}}^{I2} + \left(2 - \frac{3}{\bar{n}^{\mathcal{M}}}\right) N_{\mathcal{E}}^{I1} + 2N_{\mathcal{E}}^{I0}. \tag{6.6}$$

For example, a structured triangular mesh with $\bar{n}^{\mathcal{M}} = 6$ has $N_{\text{d.f.}} = N_{\mathcal{E}}^{I2} + (3/2)N_{\mathcal{E}}^{I1} + 2N_{\mathcal{E}}^{I0}$ which is always greater than 0 and a structured quadrilateral mesh with $\bar{n}^{\mathcal{M}} = 4$ has $N_{\text{d.f.}} = \left(\frac{1}{2}\right) N_{\mathcal{E}}^{I2} + \left(\frac{5}{4}\right) N_{\mathcal{E}}^{I1} + 2N_{\mathcal{E}}^{I0}$ which is also always greater than 0. Therefore, the existence of a set of design variables $\hat{W}_i$, $\hat{\psi}_i$, $i \in \{1, \ldots, N_{\mathcal{E}}^{I}\}$, that satisfies the design constraints is generally dependent on the inequality constraints (equations (4.16), (4.17) and (4.19)).

Another requirement is that $\mathcal{S}_0$ must not have any overlapping regions. This is needed since the reference configuration $\mathcal{S}_0$ must be planar and have no overlapping sub-domains (see §2). The following proposition provides a requirement on $\mathcal{M}$ that prevents overlaps of adjacent edge modules having a common interior node:

Proposition 6.2. *To prevent overlaps of adjacent edge modules in $\mathcal{S}_0$ associated with a common interior node in $\mathcal{M}$, the face angles associated with such an interior node must satisfy the following constraint*:

$$\phi_{jk} \leq \pi \quad \forall\, j \in \{1, \ldots, N_{\mathcal{N}}^{I}\},\ k \in \{1, \ldots, n_j^{\mathcal{M}}\}. \tag{6.7}$$

If a face angle of an interior node in $\mathcal{M}$ is concave (i.e. if $\phi_{jk} > \pi$), the edge modules connected to such an interior node overlap in $\mathcal{S}_0$, which is not allowed. Figure 17 illustrates this requirement. Overlaps in $\mathcal{S}_0$ are partially precluded provided that equation (6.7) holds for a goal mesh $\mathcal{M}$ and equation (4.17) holds for each edge module. However, no conditions preventing overlaps of edge modules not sharing a common node, nor preventing overlaps among surface sub-domains not associated with a common interior edge, are currently considered in the present design method. Nevertheless, it is shown in §8 that the considered constraints and implementation of the proposed design method successfully allow for the determination of sheet reference configurations $\mathcal{S}_0$ free of overlapping for goal meshes of various complexities.

For a determined sheet reference configuration, it is also required that $\mathcal{S}_\star$ must be a valid configuration (see definition 2.1). This requirement is partially accounted for through the edge module trimming procedure (refer to electronic supplementary material, section B) that prevents intersections of edge modules associated with a common interior node of $\mathcal{M}$. However, no constraints are currently imposed to preclude intersections of sub-domains of $\mathcal{S}_\star$ that are not associated with a common interior node in $\mathcal{M}$ at $\mathcal{S}_\star$. Nonetheless, it is also shown in §8 that the proposed design method successfully allows for the determination of goal configurations $\mathcal{S}_\star$ having no overlaps for goal meshes of various complexities.

Finally, for a determined sheet reference configuration it is required that there is a continuous set of valid configurations from the reference configuration to the goal configuration: $\{\mathcal{S}_t \mid t \in (0, t_f) \mid \mathcal{S}_{t_f} = \mathcal{S}_\star\}$. The procedure for kinematic simulation of the designed sheets to be described in §7 permits the determination of valid intermediate configurations between $\mathcal{S}_0$ and $\mathcal{S}_\star$. Although a continuous set of valid configurations is not obtained using such a numerical procedure, a discrete set containing an arbitrary number of intermediate configurations can be determined.

Regarding the uniqueness of determined sheet reference configurations, assuming that the inequality constraints in equations (4.16), (4.17) and (4.19) allow for a valid solution, such a solution is not unique because in general $N_{\text{d.f.}} > 0$ (refer to equation (6.6)). One global measure to discriminate among various design solutions and drive toward a possible unique solution is referred to as the surface area efficiency E and is defined as follows:

$$E := \frac{\text{Area}(\mathcal{M})}{\text{Area}(\mathcal{S}_0)}. \tag{6.8}$$

The numerical procedure outlined in §5 used to determine a sheet reference configuration does not consider any function to minimize or maximize (i.e. it only iteratively corrects an initial guess solution until the presented constraints are satisfied). However, other methods can be utilized to determine a sheet reference configuration that satisfies the presented constraints while optimizing a given function (e.g. maximize surface area efficiency E). Such extensions are application dependent and are recommended for future studies.

7. Determination of history of folding motion

The determination of a history of folding motion from $\mathcal{S}_0$ towards $\mathcal{S}_\star$ is considered here. The kinematic simulation approach for origami with smooth folds and its associated numerical implementation utilized herein are described in detail in [33]. The simulation of the folding motion is executed by incrementally updating the values of the fold angles using guess increments and then iteratively applying any required corrections (see [33]) such that the resulting folded configuration is valid (i.e. the kinematic constraints presented in equations (2.6)–(2.7) are met for every fold intersection). Let $\hat{\boldsymbol{\theta}}^\star \in \mathbb{R}^{3N_\mathcal{E}^I}$ be the vector constructed by collecting the values of the fold angles for each smooth fold at the goal configuration $\mathcal{S}_\star$. The goal fold angle for the interior fold of each edge module is equal to π while those for the exterior folds are equal to $-\hat{\Theta}_i/2$ (refer to figure 11). In the reference configuration $\mathcal{S}_0$, all the fold angles are equal to 0. The simulation of the sheet folding motion uses a fold and adjust approach and is performed in $N_{\text{fol}} + N_{\text{adj}}$ increments. The N_{fol} guess fold angle increments (${}^{IN}_{l}\Delta\hat{\boldsymbol{\theta}}$) are simply given as follows:

$${}^{IN}_{l}\Delta\hat{\boldsymbol{\theta}} = \frac{\hat{\boldsymbol{\theta}}^\star}{N_{\text{fol}}} \quad \forall\, l \in \{1, \ldots, N_{\text{fol}}\}. \tag{7.1}$$

As the set of fold angles at each increment is subject to iterative corrections to ensure that the kinematic constraints presented in equations (2.6)–(2.7) are met for every fold intersection, the configuration determined at the N_{fol} increment may not exactly correspond to $\mathcal{S}_\star$. Consequently, N_{adj} adjusting increments are subsequently applied. These corrective fold angle increments are calculated as follows:

$${}^{IN}_{l}\Delta\hat{\boldsymbol{\theta}} = \hat{\boldsymbol{\theta}}^\star - {}_{l-1}\hat{\boldsymbol{\theta}} \quad \forall\, l \in \{N_{\text{fol}} + 1, \ldots, N_{\text{fol}} + N_{\text{adj}}\}. \tag{7.2}$$

This framework allows for the determination of an arbitrary number ($N_{\text{fol}} + N_{\text{adj}} - 1$) of valid intermediate configurations between $\mathcal{S}_0$ to $\mathcal{S}_\star$, and represents another contribution of this work (i.e. simulation of the motion between reference and goal configurations was not addressed in related works [22,27] and it is remarked that this work is also applicable to origami with creased folds). The simple set of fold angle increments provided in equations (7.1) and (7.2) is effective for the determination of a folding motion from $\mathcal{S}_0$ to $\mathcal{S}_\star$ in all the examples presented in this work. However, it is not guaranteed to work for any arbitrary goal mesh or sheet reference configuration. For information on more complex motion planning procedures for origami the reader is referred to [42–44].

8. Implementation results

In this section, the design method for origami structures with smooth folds proposed herein is now tested against various goal meshes. The numerical solution procedure for the proposed

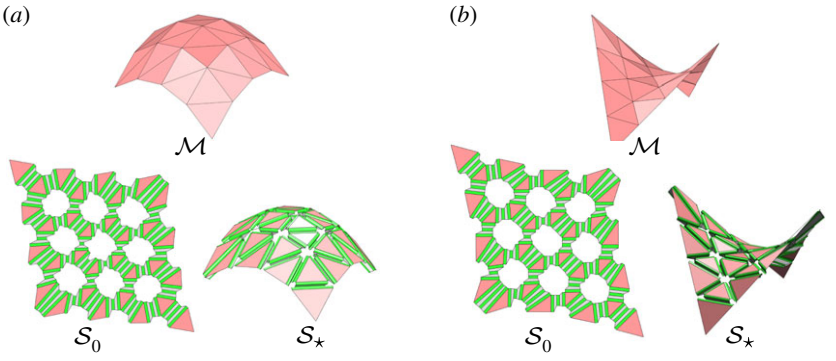

Figure 18. Polygonal meshes and their associated determined sheet reference configurations and folded goal configurations: (*a*) goal mesh of interior nodes of positive discrete Gaussian curvature; (*b*) goal mesh of interior nodes of negative discrete Gaussian curvature. (Online version in colour.)

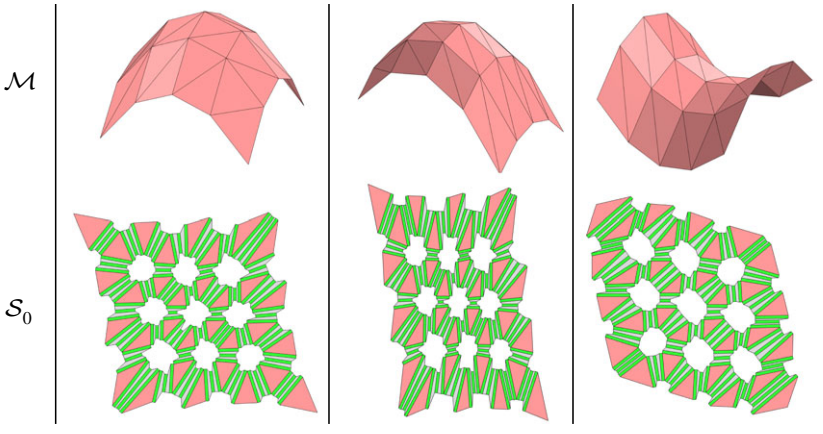

Figure 19. Various goal meshes and their determined sheet reference configurations. (Online version in colour.)

design method described in §5 and for determination of a history of folding motion outlined in §7 are implemented in MATLAB. The MATLAB three-dimensional shaded surface plot function `surf` is used to visualize the folds while the rigid faces and goal meshes are visualized through filled three-dimensional polygons using `fill3`. Smooth folds having G^2 continuity are considered in all the examples presented in this section (refer to figure 2*c*). As stated in §2a, G^2 continuity is exhibited by structures having continuous material composition and thickness across the interfaces between the faces and the smooth folds. Such a choice is taken for example purposes only and the present design method is applicable to origami structures exhibiting any other arbitrary order of geometric continuity.

The first example considers a goal mesh $\mathcal{M}$ having interior nodes of positive discrete Gaussian curvature [38,45] and is presented in figure 18*a*. A reference configuration $\mathcal{S}_0$ determined using the proposed design method and the corresponding goal configuration $\mathcal{S}_\star$ are shown in such a figure. A goal mesh having interior nodes of negative discrete Gaussian curvature is considered in figure 18*b*. Variations of the goal mesh shown in figure 18*a* and their determined sheet reference configurations are shown in figure 19. Using the kinematic simulation approach presented in §7, it is verified that each sheet reference configuration in figure 19 folds towards their corresponding goal configuration $\mathcal{S}_\star$, although not shown here for the sake of brevity.

To illustrate the non-uniqueness of determined sheet reference configurations discussed in §6, three determined sheet reference configurations associated with a single goal mesh are presented

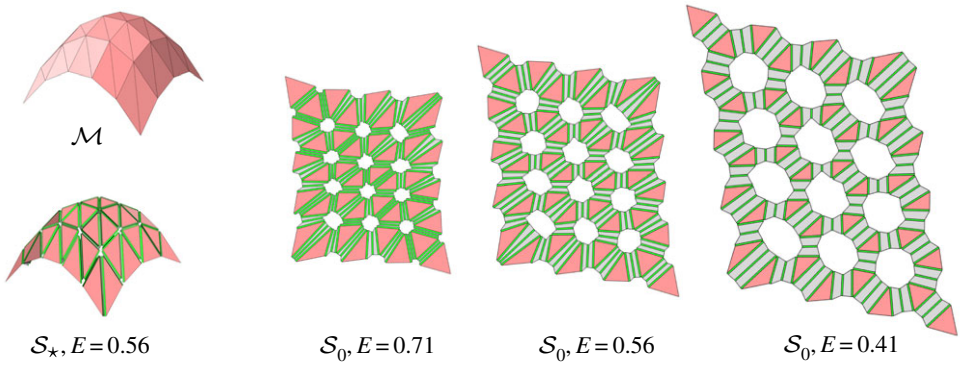

Figure 20. A goal mesh and three determined sheet reference configurations with different values of surface area efficiency E. The goal configuration $\mathcal{S}_\star$ associated with the sheet reference configuration having $E = 0.56$ is also shown. (Online version in colour.)

in figure 20. These different solutions are obtained by considering different initial guesses for the sheet design variables in the iterative solution procedure utilized in this work (described in §5). Values of surface area efficiency E, defined in equation (6.8), for the determined sheet reference configurations are also included in figure 20.

An example of a torus goal shape is provided in figure 21. Figure 21*a* shows two different discretizations of the torus goal shape. Planar sheet reference configurations for both discretizations are obtained using the proposed design method and are shown in figure 21*b*. The determined history of folding motion of one of the sheet reference configurations is shown in figure 21*c*. Furthermore, figure 21*d–f* shows the successful design/simulation results for a goal mesh associated with a sinusoidal tessellation.

It is remarked that the proposed method is not limited to triangulated meshes as the only condition on the shape of the faces in $\mathcal{M}$ is that they must be convex (see Proposition 6.2). To illustrate results for goal meshes having not all triangular faces, figure 22*a* shows an example associated with a goal mesh comprised of quadrilaterals while figure 22*b* shows the results for a goal mesh comprised of both octagons and triangles.

9. Conclusion

A novel method for the design of origami structures with smooth folds is presented in this paper. The method solves the origami design problem of determining the geometry of the planar reference configuration of a single sheet including a pattern of smooth folds that allow for the approximation of a three-dimensional goal mesh via folding. A description of the design variables, design constraints, and a numerical solution procedure are provided. Furthermore, a history of folding motion from the determined sheet reference configuration to a folded configuration that approximates the goal mesh is also determined. For origami design problems in which the goal shape is a not a polyhedral surface (e.g. a smooth surface), the process to determine a mesh discretization of such a surface before the utilization of the method presented in this paper must be addressed. Multiple algorithms for obtaining polygonal mesh discretizations of smooth surfaces are available in the literature [46,47].

A number of conclusions can be drawn based on the developed theory and the obtained results. First, the design method successfully provides fold patterns that can be realized with diverse engineering materials (e.g. metals, glassy polymers, active materials) due to the consideration of arbitrary order of continuity G^n at the folds, as opposed to G^0 creased folds idealizations available in the literature. The method was tested against goal meshes of various geometries and complexities, yielding successful results for each. Second, comprehensive origami design/simulation is achieved using the presented framework that includes both the design

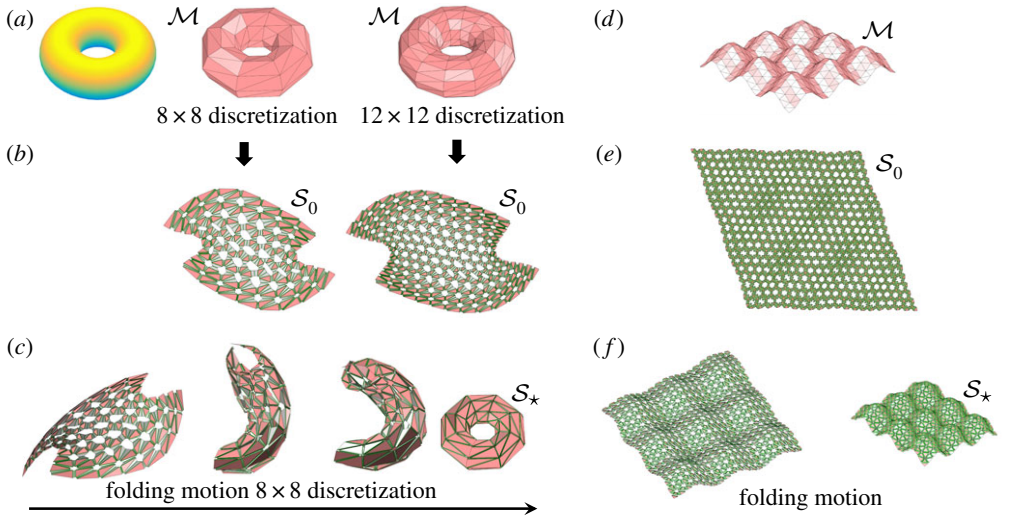

Figure 21. (*a*) Two mesh discretizations of a torus; (*b*) determined sheet reference configurations for the two discretizations shown in (*a*); (*c*) folding motion for the sheet reference configuration obtained from the 8 × 8 mesh discretization of the torus; (*d*) goal mesh representing a sinusoidal tessellation; (*e*) determined sheet reference configuration; (*f*) folding motion towards the goal configuration. (Online version in colour.)

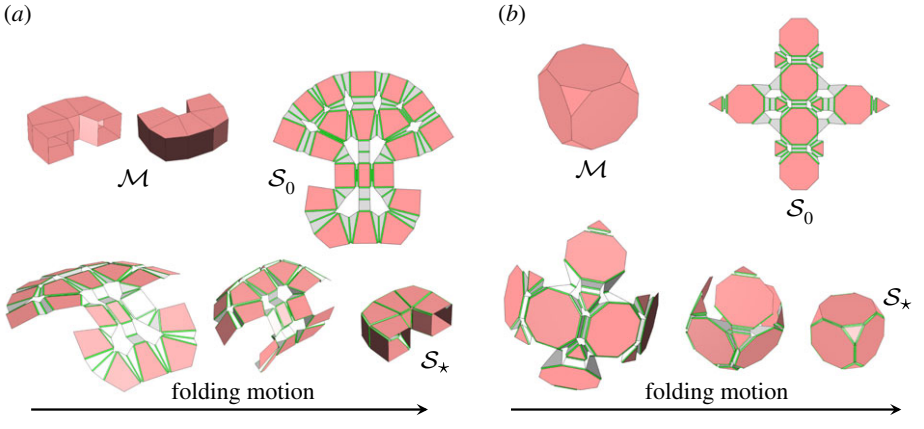

Figure 22. (*a*) Determined sheet reference configuration and folding motion associated with a goal mesh comprised of quadrilaterals. (*b*) Determined sheet reference configuration and folding motion associated with a goal mesh comprised of octagons and triangles. (Online version in colour.)

method of the sheet geometry and determination of history of folding motion. This framework allows for the determination of an arbitrary number of intermediate valid configurations between reference and goal configurations. Such a comprehensive origami design/simulation framework represents another contribution of this work and is applicable to both origami with smooth folds and conventional origami with creased folds.

Authors' contributions. E.A.P.H. developed the theory and implementation of this work, generated the results and wrote the manuscript. D.J.H. and D.C.L. developed the project, coordinated the study and provided helpful input for the research work and for the manuscript. All authors gave final approval for publication.

Competing interests. We have no competing interests.

Funding. This work is supported by the National Science Foundation and the Air Force Office of Scientific Research under grant no. EFRI-1240483. Any opinions, findings, conclusions or recommendations are those of the authors and do not necessarily reflect the views of the US Air Force.

References

1. Demaine ED, O'Rourke J. 2007 *Geometric folding algorithms*. Cambridge, UK: Cambridge University Press.
2. Lang RJ. 2007 The science of origami. *Phys. World* **20**, 30–31. (doi:10.1088/2058-7058/20/2/31)
3. Lang RJ. 2009 Computational origami: from flapping birds to space telescopes. In *Proc. of the Twenty-fifth Annual Symp. on Computational Geometry, Aarhus, Denmark, 8–10 June*, pp. 159–162. New York, NY: ACM.
4. Turner N, Goodwine B, Sen M. 2015 A review of origami applications in mechanical engineering. *Proc. Inst. Mech. Eng. Part C: J. Mech. Eng. Sci.* **230**, 0954406215597713. (doi:10.1177/0954406215597713)
5. Peraza Hernandez EA, Hartl DJ, Malak Jr RJ, Lagoudas DC. 2014 Origami-inspired active structures: a synthesis and review. *Smart Mater. Struct.* **23**, 094001. (doi:10.1088/0964-1726/23/9/094001)
6. Cromvik C, Eriksson K. 2006 Airbag folding based on origami mathematics. In *Origami 4, Fourth Int. Meeting of Origami Science, Mathematics, and Education, Pasadena, CA, 8–10 September*, pp. 129–139. Natick, MA: AK Peters.
7. Peraza Hernandez EA, Hu S, Kung HW, Hartl D, Akleman E. 2013 Towards building smart self-folding structures. *Computers Graphics* **37**, 730–742. (doi:10.1016/j.cag.2013.05.022)
8. Shaar NS, Barbastathis G, Livermore C. 2015 Integrated folding, alignment, and latching for reconfigurable origami microelectromechanical systems. *J. Microelectromech. Syst.* **24**, 1043–1051. (doi:10.1109/JMEMS.2014.2379432)
9. Filipov ET, Paulino GH, Tachi T. 2016 Origami tubes with reconfigurable polygonal cross-sections. *Proc. R. Soc. A* **472**, 20150607. (doi:10.1098/rspa.2015.0607)
10. Saintsing CD, Cook BS, Tentzeris MM. 2014 An origami inspired reconfigurable spiral antenna. In *Proc. of ASME 2014 IDETC/CIE, Buffalo, NY, 17–20 August*, pp. V05BT08A050. New York, NY: American Society of Mechanical Engineers.
11. Bassik N, Stern GM, Gracias DH. 2009 Microassembly based on hands free origami with bidirectional curvature. *Appl. Phys. Lett.* **95**, 091901. (doi:10.1063/1.3212896)
12. Shin B, Felton SM, Tolley MT, Wood RJ. 2014 Self-assembling sensors for printable machines. In *Proc. of the 2014 IEEE Int. Conf. on Robotics and Automation* (*ICRA*), *Hong Kong, 31 May–5 June*, pp. 4417–4422. Piscataway, NJ: IEEE.
13. Early JT, Hyde R, Baron RL. 2004 Twenty-meter space telescope based on diffractive Fresnel lens. In *Proc. of the SPIE's 48th Annual Meeting, Optical Science and Technology. Int. Soc. for Optics and Photonics, San Diego, CA*, pp. 148–156. Bellingham, WA: SPIE.
14. Song Z *et al.* 2014 Origami lithium-ion batteries. *Nat. Commun.* **5**, 3140. (doi:10.1038/ncomms4140)
15. Miyashita S, Guitron S, Ludersdorfer M, Sung CR, Rus D. 2015 An untethered miniature origami robot that self-folds, walks, swims, and degrades. In *Proc. of the 2015 IEEE Int. Conf. on Robotics and Automation* (*ICRA*), *Seattle, WA: 26–30 May*, pp. 1490–1496. Piscataway, NJ: IEEE.
16. Martínez-Martín FJ, Thrall AP. 2014 Honeycomb core sandwich panels for origami-inspired deployable shelters: multi-objective optimization for minimum weight and maximum energy efficiency. *Eng. Struct.* **69**, 158–167. (doi:10.1016/j.engstruct.2014.03.012)
17. Kuribayashi K, Tsuchiya K, You Z, Tomus D, Umemoto M, Ito T, Sasaki M. 2006 Self-deployable origami stent grafts as a biomedical application of Ni-rich TiNi shape memory alloy foil. *Mater. Sci. Eng. A* **419**, 131–137. (doi:10.1016/j.msea.2005.12.016)
18. Lebée A. 2015 From folds to structures, a review. *Int. J. Space Struct.* **30**, 55–74. (doi:10.1260/0266-3511.30.2.55)
19. Tachi T. 2009 Simulation of rigid origami. In *Origami 4, Fourth Int. Meeting of Origami Science, Mathematics, and Education, Pasadena, CA, 8–10 September*, pp. 175–187. Natick, MA: AK Peters.
20. Belcastro SM, Hull TC. 2002 Modelling the folding of paper into three dimensions using affine transformations. *Linear Algebra and its Applications* **348**, 273–282. (doi:10.1016/S0024-3795(01)00608-5)
21. Belcastro SM, Hull TC. 2002 A mathematical model for non-flat origami. In *Origami 3: Third Int. Meeting of Origami Mathematics, Science, and Education, Asiloma, CA*, pp. 39–51. Natick, MA: AK Peters.
22. Tachi T. 2010 Origamizing polyhedral surfaces. *IEEE Trans. Visualization Computer Graphics* **16**, 298–311. (doi:10.1109/TVCG.2009.67)

23. Lang RJ. 1996 A computational algorithm for origami design. In *Proc. of the Twelfth Annual Symp. on Computational Geometry, Philadelphia, PA, 24–26 May*, pp. 98–105. New York, NY: ACM.
24. Evans TA, Lang RJ, Magleby SP, Howell LL. 2015 Rigidly foldable origami gadgets and tessellations. *R. Soc. open sci.* **2**, 150067. (doi:10.1098/rsos.150067)
25. Zhou X, Wang H, You Z. 2015 Design of three-dimensional origami structures based on a vertex approach. *Proc. R. Soc. A* **471**, 20150407. (doi:10.1098/rspa.2015.0407)
26. Schlickenrieder W. 1997 *Nets of polyhedra*. Berlin, Germany: Technische Universität.
27. Tachi T. 2009 3D origami design based on tucking molecule. In *Origami 4, Fourth Int. Meeting of Origami Science, Mathematics, and Education, Pasadena, CA, 8–10 September*, pp. 259–272. Natick, MA: AK Peters.
28. Tachi T. 2013 Designing freeform origami tessellations by generalizing Resch's patterns. *J. Mech. Des.* **135**, 111006. (doi:10.1115/1.4025389)
29. Saito K, Tsukahara A, Okabe Y. 2016 Designing of self-deploying origami structures using geometrically misaligned crease patterns. *Proc. R. Soc. A* **472**, 20150235. (doi:10.1098/rspa.2015.0235)
30. Upadhe SN, Chavan AS, Shaikh TB. 2014 Industrial origami a review. *Int. J. Innov. Res. Adv. Eng.* **1**, 265–269.
31. Peraza-Hernandez E, Hartl D, Galvan E, Malak R. 2013 Design and optimization of a shape memory alloy-based self-folding sheet. *J. Mech. Des.* **135**, 111007. (doi:10.1115/1.4025382)
32. Mailen RW, Liu Y, Dickey MD, Zikry M, Genzer J. 2015 Modelling of shape memory polymer sheets that self-fold in response to localized heating. *Soft Matter* **11**, 7827–7834. (doi:10.1039/C5SM01681A)
33. Peraza Hernandez EA, Hartl DJ, Lagoudas DC. 2016 Kinematics of origami structures with smooth folds. *J. Mech. Robotics* **8**, 061019. (doi:10.1115/1.4034299)
34. Peraza Hernandez EA, Hartl DJ, Akleman E, Lagoudas DC. 2016 Modeling and analysis of origami structures with smooth folds. *Computer-Aided Design* **78**, 93–106. (doi:10.1016/j.cad.2016.05.010)
35. Wheeler CM, Culpepper ML. 2016 Soft origami: classification, constraint, and actuation of highly compliant origami structures. *J. Mech. Robotics* **8**, 051012. (doi:10.1115/1.4032472)
36. Kwok TH, Wang CCL, Deng D, Zhang Y, Chen Y. 2015 Four-dimensional printing for freeform surfaces: design optimization of origami and kirigami structures. *J. Mech. Design* **137**, 111413. (doi:10.1115/1.4031023)
37. Barsky BA, DeRose TD. 1984 *Geometric continuity of parametric curves*. San Francisco, CA: Computer Science Division, University of California.
38. Akleman E, Chen J. 2006 Insight for practical subdivision modeling with discrete Gauss-Bonnet theorem. In *Int. Conf. on Geometric Modeling and Processing, Pittsburg, PA, 26–28 July* (eds M-S Kim, K Shimada), pp. 287–298. Berlin, Germany: Springer.
39. Tachi T. 2010 Freeform variations of origami. *J. Geom. Graph* **14**, 203–215.
40. Erickson J, Har-Peled S. 2004 Optimally cutting a surface into a disk. *Discrete Comput. Geometry* **31**, 37–59. (doi:10.1007/s00454-003-2948-z)
41. Sullivan JM. 2008 Curvatures of smooth and discrete surfaces. In *Discrete Differential Geometry*. Berlin, Germany: Springer, pp. 175–188.
42. Song G, Amato NM. 2004 A motion-planning approach to folding: from paper craft to protein folding. *IEEE Trans. Robotics Autom.* **20**, 60–71. (doi:10.1109/TRA.2003.820926)
43. Xi Z, Lien JM. 2015 Plan folding motion for rigid self-folding machine via discrete domain sampling. In *2015 IEEE Int. Conf. on Robotics and Automation* (*ICRA*), *Seattle, WA: 26–30 May*, pp. 2938–2943. Piscataway, NJ: IEEE.
44. Xi Z, Lien JM. 2015 Folding and unfolding origami tessellation by reusing folding path. In *2015 IEEE Int. Conf. on Robotics and Automation* (*ICRA*), *Seattle, WA, 26–30 May*, pp. 4155–4160. Piscataway, NJ: IEEE.
45. Calladine CR. 1989 *Theory of shell structures*. Cambridge, UK: Cambridge University Press.
46. Frey PJ, George PL. 2008 *Mesh generation: application to finite elements*, 2nd edn. Hoboken, NJ: ISTE/John Wiley & Sons.
47. Zheng Y, Lewis RW, Gethin DT. 1996 Three-dimensional unstructured mesh generation: Part 2. Surface meshes. *Computer Methods Appl. Mech. Eng.* **134**, 269–284. (doi:10.1016/0045-7825(95)00917-5)